MASTER THESIS

Microfluidic Cell Concentration and Threshold Identification

Submitted at the Faculty of Electrical Engineering, Vienna University of Technology
in partial fulfillment of the requirements for the degree of
Master of Sciences (Diplomingenieur)

under supervision of

Univ.Prof. Dr. Franz Keplinger
Dipl.-Ing. Dietmar Puchberger-Enengl

by

Ulrich Schneider
Matr.Nr. 9725477
Hochbergstraße 7, 2380 Perchtoldsdorf

November, 2015

Abstract

Microfluidic devices offer a wide range of improvements over legacy applications as well as entirely new uses. The purpose of this work is to address a diagnostic need regarding wound infections, which are predominantly caused by only a few bacterial strains, by demonstrating a combination of methods capable of extracting, washing and detecting these pathogens. Considering the electrophoretic mobility of bacteria [PVH+12], the primary extraction mechanism was thus chosen to be DC electrophoresis, with electroosmotic flow (EOF) serving to provide a counter flow, separating live cells from any debris and residue contained in the sample. Collection of target cells will take place in any location where fluid velocity exceeds the target cell migration speed in the local electric field, which can be achieved in a gradual constriction within the channel, resembling a funnel. Ideally, the electric properties of this structure should be indistinguishable from those of the working fluid, leaving the electric field profile unaltered, which initially suggests the use of a hydrogel as a building material. However, issues arising from geometric precision, materials compatibility and a parallel current path bypassing the constriction strongly indicate the use of a narrow slab of substrate instead. The described setup depends on the electrolyte ion concentration, which must be tuned to a band where cell movement occurs within the channel, but not through the nozzle.

Table of Contents

Nomenclature

E	electric field strength
I	electric current
J	electric current density
g	gravitational acceleration
L	length
M	mass
t	time
F	force
T	temperature
u	velocity
V	volume
$\dot{\mathrm{V}}$	volume flow
Re	*Reynolds* number
Kn	*Knudsen* number
Pe	*Peclet* number
Bo	*Bond* number
Ca	*Capillary* number
We	*Weber* number
Pr	*Prandtl* number
$\mathrm{D_H}$	hydraulic diameter
σ	electric conductivity
ϵ	dielectric permittivity

λ	*Debye* length
η	dynamic viscosity
υ	kinematic viscosity
ρ	density
τ	time scale
T_S	surface tension
R	viscous drag
ζ	Zeta-potential
L_{mfp}	mean free path
k_B	*Boltzmann* constant
PCC, ρ_P	*Pearson* correlation coefficient
CM	*Clausius-Mossotti* factor
DC	direct current
AC	alternating current
EP	electrophoresis
DEP	dielectrophoresis
EOF	electro-osmosic flow
EDL	electric double layer
AO	acridine orange
PEG	polyethyleneglycol diacrylate
HMPP	2-hydroxy-2-methylpropiophenone
PGMEA	propylene glycol methyl ether acetate
PDMS	polydimethylsiloxane
PVA	polyvinyl alcohol
SI	international system of units
C	constant

1 Introduction

Cell detection and identification are integral tasks in many biomedical applications, with a wide range of methods available to suit applications, such as pathogen or tumor cell detection. Classical methods for cell detection rely on selective culturing, gram staining and biochemical testing [LAF+14] with long incubation times, comparably large sample volumes and elaborate protocols. Many of these issues can directly be addressed through the adoption of microfluidic platforms [PVH+12]. As implied, the characteristics of these devices are feature sizes in the sub-mm range, facilitating the integration of complementary functionalities into a single unit as well as parallelization. Advantages in processing include accelerated diffusion and mixing, minimal sample and reagent consumption as well as avoiding cross contamination through single use. In terms of mobility and flexibility, a distinction has to be made between self contained units and cartridges used in a base station containing reusable components, which remain isolated from sample fluids and are therefore subjected to a smaller degree of wear and attrition, such as optical transducers, power supply and other electronic hardware [SNO+12]. Both approaches have their respective of advantages and disadvantages, which are mainly related to initial and running costs, although virtually all devices designed so far rely on external read out equipment, there are notable exceptions like a fully contained, saliva based immunoassay demonstrated by *Liu et al.* [LQO+09]. A fully integrated Lab-on-a-Chip (LoC) is naturally the most flexible option in a Point-of-Care (PoC) context, which is probably one of the most compelling arguments in favor of the technology [RZA12], but not for routine work, where a large number of tests tends to favor the separate solution.

The two main principles of operating microfluidic devices are continuous flow and droplet-based operation. The former regularly relies on externally supplied pressure (e.g. micro-pumps [GJZ+12]) or capillary filling where the working fluid characteristics and channel geometry permit it. In an attempt to retain direct pressure control while avoiding inter-

facing issues between an external pump and a chip smaller than a finger nail, centrifugal pumping on a rotating compact disc (CD) has found some application [RLH+11]. The latter uses discrete droplets, to process volumes in the nanolitre range, sometimes referred to as *digital microfluidics* [Cha05]. Although the advantages of handling droplets are numerous, especially programmability [SAHZ13] and ease of testing [RRDB12], initial preparatory steps like extraction, concentration and enrichment lend themselves to continuous operation [RMW95], where a higher throughput can be obtained using inherently parallel techniques, such as Pinch-Flow-Fractionation [VK08] or hydrophoresis [CP07]. Detection normally follows a concentrating step and is often performed via absorptive or reflective optical tests. Even integrated microscopy [HEB+06], surface enhanced *Raman* scattering (SERS [QN08]), or more conveniently, electric impedance spectroscopy (EIS [SM10]) have been demonstrated. In addition, magnetic cell separators exist, which either exploit the intrinsic properties of target cells [HF05] or have to resort to labeling with adhesive magnetic particles [AKS08], as do acoustic sensors, where a mass of cells affects the resonant properties of a quartz-crystal micro balance (QCM [SL05]).

Many impedance based LoCs rely on binding or trapping via antibodies onto a surface, whose area can be increased by e.g. interdigitated geometry [VL09] [RA05] at given outer dimensions. Other designs avoid the need for antibody coating by employing electrophoresis (EP [MMP97] [SLR72]) in order to reversibly deposit bacteria on a barrier [PEPH+11] [NMF+09], e.g. a slab of hydrogel, whose electric properties closely mimic those of the working fluid. *Church et al.* presented a design with a narrow constriction that enables selective cell concentration and lysis based on differing (di)electrophorectic mobilities [CZH+10]. Although bearing some resemblance to the device created in this work, it does not put emphasis on accurate cell positioning for better read-out or managing electric stress at the point of collection. Cytometric approaches are also in use, such as a miniaturized *coulter counter* [ZT06], which, like their full scale equivalents, only process one particle at a time.

Despite increasing maturity, the spread of commercially available microfluidic devices appears to have remained sluggish [PVH+12]. Even though manufacturing techniques currently in use were developed for small batches and are more amenable prototyping rather than mass production, giving rise to issues like increased module spread [Ker07], technological limitations alone can not account for this reluctance in uptake as e.g. the satisfactory field trial of an integrated enzyme-linked immunosorbent assay (ELISA) called *mChip* [CLC+11] illustrates. Procedurally, established laboratory protocols, which are required for quality control and standardization, are unsurprisingly geared heavily towards existing

techniques and the willingness to deviate from an already working system is often limited [RZA12].

With the unclear and protracted introduction of microfluidic devices in mind, a choice was made early in this work to rely only on intrinsic fluid and cell properties along with geometry to minimize complexity and provide a wide possible choice of building materials. Any insulator, which generates an electro-osmotic flow (EOF) in conjunction with the buffer solution will serve. EOF itself can be incorporated into the functionality of the design, to simplify the preparation of fluids and to help preserve the viability of cells, since most chemicals used to suppress EOF are biocides [PEPH+11]. Sensing can be performed by any technique that is capable of bulk detection, such as optics, sensing electrodes or by direct measurement of the voltage and impedance along the length of the microchannel caused by the EP driving current. At the first glance, this longitudinal measurement is very attractive, as it obviates the need for accurately placed insulated sensing electrodes. This advantage, however, comes at the cost of versatility, since hundreds of volts are often reached, which complicates the additional use of frequency based, detailed impedance spectroscopic assay, due to hardware constraints. A source capable of modulating these voltages at a sufficiently high frequency went beyond the tools available in the context of this work.

2 Theory

In principle, three mechanisms suffice to describe the function of the cell concentrator: electrophoresis, drag and electro-osmotic flow (EOF). A dielectrophoretic (DEP) influence exists, due to the inevitable field gradient arising from a constriction, which actually helps device functionality, as shown in section 2.1.4. While cell properties are subject to variation, EOF can be modeled analytically. Using dimensional analysis, the desired expressions can be derived quickly, with the exception of a multiplicative factor, which has to be determined by other means, such as an experiment. Another benefit of this approach is that the dimensionless parameters used to derive these expressions reveal many characteristic properties of the designed system. One of the most prominent examples in fluidic applications is given by the *Reynolds* number *Re* (Section 2.1.2.3), whose value allows to distinguish between laminar and turbulent flow regimes.

2.1 Dimensional Analysis

According to the *Theorem of Dimensional Homogeneity* [Bri31], a physical quantity is always dimensionally a power law monomial of the form

$$Q = C\ M^a L^b t^c I^d \theta^e S^f \tag{2.1}$$

with a through f and constant factor C being real numbers and M, L, t, I, θ and S denoting mass, length, time, electric current, temperature and luminosity, respectively. Using these SI dimensions is by no means a requirement and can actually complicate matters, with certain problems benefiting e.g. from using a dimension of force rather than deriving it from M, L and t or a mass-less system in an astronomical context [Spu92].

The most important step [PS13] is to identify a complete set of independent variables q_i which determine the value of a dependent variable of interest, Q:

$$Q = f(q_1, q_2, ...q_n) \tag{2.2}$$

Such a relationship of n independent variables with k dimensions can alternatively be expressed [Son01] using $n - k$ dimensionless quantities as:

$$\pi = f(q_1, q_2, ...q_n; \pi_1, \pi_2, ...\pi_{n-k}) \tag{2.3}$$

with π_i a complete, dimensionless subset of the original independent variables q_i. Since their dimension is 1 and *Dimensional Homogeneity* [Bri31] requires that any relation between physical quantities be dimensionally consistent, the variables q_i have to be absent, resulting in *Buckingham's Theorem* [Buc14], which states:

> For a given physical effect or process where there are n physically relevant variables that can be described by k fundamental dimensions, there are a total of $n - k$ independent, dimensionless quantities, called *Pi-Groups*, π_1, π_2,.... π_{n-k}. The behavior of the effect or process can be described by the dimensionless equation 2.4

$$\pi = f(\pi_1, \pi_2, ...\pi_{n-k}) \tag{2.4}$$

Understanding the problem and identifying all physically relevant independent variables as well as the desired dependent variable is strictly necessary to obtain a solution. In cases, where the modeling remains incomplete, the resulting set of equations will only have a trivial solution. Once obtained, individual *Pi-Groups* can be multiplied and divided freely due to their dimensionless nature, to help suit the modeling, conventions or compatibility with previous work and data. They are, therefore, not unique. The reduction to $n - k$ terms, combined with their independence from units of measurement make them highly efficient for purposes of comparing and mapping a wide range of problems, in order to determine the relationship between physical mechanisms in the context of a given task and facilitate the modeling process. For this purpose, often occurring dimensionless parameters are named after their discoverers and used to characterize a given problem. Some important non-dimensional numbers in the context of microfluidics are provided in Section 2.1.2.

2.1.1 Application

As an initial example, an expression proportional to the characteristic depth (*Debye* Length) of the Electric Double Layer (EDL) can be derived quickly by applying this method. This double layer arises from a compact layer of charges accumulating near a liquid to solid interface being screened by a diffuse cloud of counter-ions within the liquid. While the compact layer will remain tightly bound by electrostatic attraction, the diffuse half will react to an electric field and subsequently drag the bulk of the liquid along, resulting in electro-osmotic flow [YIB06]. One advantage of EOF is that it offers a uniform flow profile (*plug flow*) compared to the parabolic one associated with purely pressure driven flow in a microchannel.

As a starting point, the dependent variable of interest clearly has the dimension of length and is expected to be influenced by fluid permittivity, free ion concentration and charge, but to arrive at a solution, maybe less obvious, thermo-kinetic aspects represented by absolute temperature and the *Boltzmann* constant have to enter the picture, as shown in Table 2.1.

Variables					
depth λ	Boltzmann constant k_B	temperature T	permittivity ϵ	ion density n_0	charge z e
L	$M\,L^2\,t^{-2}\,\theta^{-1}$	θ	$M^{-1}\,L^{-3}\,t^4\,I^2$	L^{-3}	I t

Table 2.1: Dimensional table for the *Debye* length

Comparing the numbers of variables an dimensions (n = 6, k = 5) only one dimensionless quantity can be found, allowing to set the exponent of the sought-after variable to one and temperature is only part of two entries, which can therefore be combined beforehand, leading to Eq. 2.5 and Eq. 2.6.

$$\pi = \lambda(k_B T)^a \epsilon^b {n_0}^c (ze)^d \tag{2.5}$$

dimensionally, this means

$$L^0 M^0 t^0 I^0 \theta^0 = L \left(\frac{ML^2}{t^2}\right)^a \left(\frac{t^4 I^2}{ML^3}\right)^b \left(\frac{1}{L^3}\right)^c (It)^d \tag{2.6}$$

Solving for real numbers a, b, c, d yields a = b = $-1/2$, c = 1 and d = $1/2$ in Eq. 2.7:

$$\pi = \lambda \sqrt{\frac{n_0 z^2 e^2}{\epsilon k_B T}} \tag{2.7}$$

where

$$F\left(\lambda \sqrt{\frac{n_0 z^2 e^2}{\epsilon k_B T}}\right) = 0 \tag{2.8}$$

or

$$\lambda = C \sqrt{\frac{\epsilon k_B T}{n_0 e^2 z^2}} \tag{2.9}$$

An analytical solution reveals a value of the multiplicative factor of $1/\sqrt{2}$ [WCW07], which is hardly relevant when comparing the layer thickness in the nm range to the size of a microchannel.

In the same fashion, expressions for electro-osmotic flow (EOF) velocity can be obtained. Again, fluid permittivity will play a pivotal role along with an electric field driving the EOF, while viscosity will certainly be a factor due to fluid motion. One quantity remains, the Zeta-potential [SERL03], an important parameter in problems including liquid to solid interfaces describing the electrostatic potential between the diffuse and compact portions of the EDL, which is mentioned in the beginning of Section 2.1.1. The Zeta-potential can not be measured directly but has to be derived from known fluid properties along with flow velocity measurements, where temperature also plays a significant role [VXL06].

Variables				
velocity u	permittivity ϵ	Zeta-potential ζ	viscosity η	electric field E
$\mathrm{L\,t^{-1}}$	$\mathrm{M^{-1}\,L^{-3}\,t^4\,I^2}$	$\mathrm{M\,L^2\,t^{-3}\,I^{-1}}$	$\mathrm{M\,L^{-1}\,t^{-1}}$	$\mathrm{M\,L\,t^{-3}\,I^{-1}}$

Table 2.2: Dimensional table for EOF dependent on electric field

Using Table 2.2, Eq. 2.10 can be formed:

$$L^0 M^0 t^0 I^0 = \frac{L}{t}\left(\frac{t^4 I^2}{M L^3}\right)^a \left(\frac{M L^2}{t^3 I}\right)^b \left(\frac{M}{L t}\right)^c \left(\frac{M L}{t^3 I}\right)^d \tag{2.10}$$

and solved by $a = b = d = -1$ and $c = 1$, therefore:

$$\pi = u\frac{\eta}{\epsilon\zeta E} \tag{2.11}$$

yielding

$$u = C\ \frac{\epsilon\zeta E}{\eta} \tag{2.12}$$

The *Helmholtz-Smoluchowski* solution derived from balancing electric and viscous drag forces shows the constant factor to equal 1 [CCST10].

If the electric field is provided by constant amperage, replacing the electric field strength with current density is desirable. In this case conductivity is required to complete the model according to Table 2.3, $n = 6$ and $k = 4$, therefore two independent dimensionless terms exist. By contrast, applying *Ohm's Law* $J = \sigma E$ to Eq. 2.12 will only reveal a part of Eq. 2.17.

Variables					
velocity u	permittivity ϵ	Zeta-potential ζ	viscosity η	conductivity σ	current density J
$L\,t^{-1}$	$L^{-3}\,t^{4}\,M^{-1}\,I^{2}$	$M\,L^{2}\,t^{-3}\,I^{-1}$	$M\,L^{-1}\,t^{-1}$	$M^{-1}\,L^{-3}\,t^{3}\,I^{2}$	$L^{-2}\,I$

Table 2.3: Dimensional table for EOF at constant current

$$L^0M^0t^0I^0 = \left(\frac{L}{t}\right)^a\left(\frac{t^4I^2}{ML^3}\right)^b\left(\frac{ML^2}{t^3I}\right)^c\left(\frac{M}{Lt}\right)^d\left(\frac{t^3I^2}{ML^3}\right)^e\left(\frac{I}{L^2}\right)^f \tag{2.13}$$

Solving for exponents a through f reveals $a_1 = d_1 = e_1 = 1,\ b_1 = c_1 = f_1 = -1$ and $a_2 = 0,\ b_2 = f_2 = 1,\ c_2 = 0,\ d_2 = -1/2,\ e_2 = -3/2$, with the resulting *Pi-Groups* in Eq. 2.14 and Eq. 2.15:

$$\pi_1 = \frac{u\eta\sigma}{\epsilon\zeta J} \tag{2.14}$$

$$\pi_2 = \frac{\epsilon J}{\sqrt{\eta\sigma^3}} \tag{2.15}$$

These groups are part of the implicitly defined function

$$F\left(\frac{u\eta\sigma}{\epsilon\zeta J}, \frac{\epsilon J}{\sqrt{\eta\sigma^3}}\right) = 0 \tag{2.16}$$

from which an expression for u of the form

$$u = C\ \left(\frac{\epsilon\zeta J}{\eta\sigma}\right) f\left(\frac{\epsilon J}{\sqrt{\eta\sigma^3}}\right) \tag{2.17}$$

is obtained. As mentioned in the introduction (Section 2.1), these solutions are not unique and while the given solution highlights the similarities between the electric field (E) and current density (J) based models, another solution is $a_1 = 1, d_1 = 1/2, c_1 = -1$, $d_1 = -1/2$, $b_1 = f_1 = 0$ with coefficients a_2 through f_2 remaining the same as before. The corresponding *Pi-Groups* are

$$\pi_1' = \frac{u\sqrt{\eta}}{\zeta\sqrt{\sigma}} \tag{2.18}$$

$$\pi_2' = \frac{\epsilon J}{\sqrt{\eta\sigma^3}} \tag{2.19}$$

with u being

$$u = C\ \left(\frac{\zeta\sqrt{\sigma}}{\sqrt{\eta}}\right) f\left(\frac{\epsilon J}{\sqrt{\eta\sigma^3}}\right) \tag{2.20}$$

Note that $\pi_1' = \pi_1\pi_2$. Although the exact nature of function $f(\pi_2)$ cannot be determined by this method, any given value of the term π_2 will return the same result without regard to the actual composition of the *Pi-Group* π_2. This allows keeping it constant over a wide range of physical parameters, by adjusting the more accessible factors, i.e. current density, a method, which, when applied to every dimensionless term, will leave the system behavior identical.

Another detail of interest is the liquid throughput in a channel under pressure. Even though external pumps are absent in the design, surface tension and small height differences between reservoirs can cause changes in the flow in either direction. Additionally, this

serves as an example of a system including a dimension of force rather than mass, seen in Table 2.4.

Variables			
flow $\dot{V}$	pressure gradient dp	viscosity η	hydraulic diameter D_H
$L^3\,t^{-1}$	$L^{-3}\,F$	$L^{-2}\,F\,t$	L

Table 2.4: Dimensional table for volume flow

With n = 4 and k = 3, the solution of Eq. 2.21 involves one *Pi-Group*. More on the concept of the hydraulic diameter D_H can be found in Section 2.1.2.

$$L^0F^0t^0 = \frac{L^3}{t}\left(\frac{F}{L^3}\right)^a\left(\frac{Ft}{L^2}\right)^b L^c \tag{2.21}$$

a = −1, b = 1 and c = −4, so

$$\pi = \frac{\dot{V}\eta}{D_H^4 dp} \tag{2.22}$$

$$\dot{V} = C\,\frac{D_H^4 dp}{\eta} \tag{2.23}$$

The constant C in question has a value of $\pi/128$, according to an analytical solution known as *Hagen-Poiseuille* equation [Spu92].

Target cells are modeled as spherical particles with a diameter d_P and subjected to viscous (*Stokes*) drag R.

Variables				
drag R	velocity u	viscosity η	density ρ	diameter d_P
$L\,M\,t^{-2}$	$L\,t^{-1}$	$M\,L^{-1}\,t^{-1}$	$M\,L^{-3}$	L

Table 2.5: Dimensional table for particle drag

Here, n = 5 and k = 3, so two *Pi-Groups* exist.

$$L^0M^0t^0 = \left(\frac{LM}{t^2}\right)^a \left(\frac{L}{t}\right)^b \left(\frac{M}{Lt}\right)^c \left(\frac{M}{L^3}\right)^d L^e \tag{2.24}$$

which can be solved by $a_1 = d_1 = 1, b_1 = 0, c_1 = -2, a_2 = 0, b_2 = d_2 = e_2 = 1$ and $c_2 = -1$, therefore

$$\pi_1 = \frac{R\rho}{\eta^2} \tag{2.25}$$

$$\pi_2 = \frac{u\rho d_P}{\eta} \tag{2.26}$$

and

$$R = C\ \frac{\eta^2}{\rho} f\left(\frac{u\rho d_P}{\eta}\right) \approx C\ \eta u d_P \tag{2.27}$$

With π_2 being the *Reynolds* number *Re* from Section 2.1.2.3 and examining the special case of very low *Re*, which is justified in the case of laminar flow, $f(\pi_2)$ is approximated as π_2), yielding Eq. 2.27. The constant C in question actually has the value 3π [Spu92].

2.1.2 Characteristic Dimensionless Parameters

Within the context of microfluidics, several dimensionless expressions are routinely used to determine the characteristics of a system, identifying dominant physical mechanisms with corresponding design implications [PS13].

Consistent input is achieved through adherence to conventions like for example the definition of *hydraulic diameter* D_H for channels of different cross sections. Many dimensionless parameters include a characteristic length, which in the case of a circular cross section is straightforward, its diameter d. A more general approach is relating area to circumference, whose values are $A = \frac{d^2}{4}\pi$ and $C = d\pi$ in the circular case, which means that a factor of four is also required for this comparison. In cases where D_H varies with channel length, maximum and minimum values have to be considered.

$$D_H = \frac{4 \cdot Area}{Wetted\ Perimeter} \tag{2.28}$$

Another important area are characteristic time scales, where four different ones are regularly used [PS13]. L is again a characteristic length, u denotes flow velocity, η dynamic viscosity, $\upsilon = \eta/\rho$ kinematic viscosity, ρ mass density and T_S surface tension.

- *Convective*: time scale for propagation of flow perturbations in a liquid

$$\tau_C = \frac{L}{u} \tag{2.29}$$

- *Diffusive*: propagation by random molecular motion alone

$$\tau_D = \frac{L^2\rho}{\eta}\left(= \frac{L^2}{\upsilon}\right) \tag{2.30}$$

- *Capillary*: time to regain interface geometry under influence of viscosity

$$\tau_{Ca} = \frac{\eta L^2}{T_S} \tag{2.31}$$

- *Rayleigh Time Scale*: characteristic of a perturbed interface induced by inertia and surface tension

$$\tau_{Ra} = \sqrt{\frac{\rho L^3}{T_S}} \tag{2.32}$$

2.1.2.1 Knudsen Number

The *Knudsen* number is based on a comparison between a characteristic length L of a system (typically D_H) and the mean free path of molecular motion, which is calculated as

$$L_{mfp} = \frac{k_B T}{\sqrt{2} p d^2 \pi} \tag{2.33}$$

with k_B, T, p and d denoting the *Boltzmann* constant, absolute temperature, absolute pressure and molecular diameter. The value of *Kn*

$$Kn = \frac{L_{mfp}}{L} \tag{2.34}$$

indicates whether molecules interact more often with one another or rather the system boundaries. In case of the latter, continuum mechanics become increasingly inappropriate and have to be amended with discontinuous elements and eventually replaced by simulation [PS13]. The corresponding value bands are summarized in Table 2.6.

Knudsen Number	
$Kn < 10^{-3}$	normal continuum model, with zero-slip boundary conditions
$10^{-3} < Kn < 0.1$	continuum model with limited boundary slip
$0.1 < Kn < 10$	*mesoscale*, continuum approximation needs supplemental discrete, molecular modeling
$Kn > 10$	particle-based methods only

Table 2.6: Significance of the *Knudsen* number

In microfluidic applications with channel dimensions in the micrometer range and liquids with mean free path in the sub-nm range of molecule size, the resulting range of Kn indicates that the continuum model is applicable.

2.1.2.2 Peclet Number

Molecular transport in fluids results from a combination of random, thermal motion (diffusion) dependent on solvent and solute properties, as well as absolute temperature (which is included in diffusion coefficient D) and bulk flow, typified by velocity u. The relative importance of these mechanisms is expressed in the *Peclet* number:

$$Pe = \frac{uL}{D} \tag{2.35}$$

As before, L is a characteristic length of the system, D_H in the case of a channel.

If Pe remains below approximately 1000, diffusion provides a sizable contribution, which has implications for e.g. blending and mixing operations. Diffusion should be employed rather than stirring in a low Pe design [PS13], indicating whether it is more advantageous to blend fluids within channels in one pass or to rely on vortices for that purpose. The concept can include suspended particles as well, in which case D can be derived using the *Stokes-Einstein* relation Eq. 2.36, where η denotes the viscosity of the fluid, d_P the particle diameter, k_B the *Boltzmann* constant and T is the temperature in *Kelvin*.

$$D = \frac{k_B T}{3\pi\eta d_P} \tag{2.36}$$

2.1.2.3 Reynolds Number

All fluid flow can be separated into laminar and turbulent flow regimes. In case of the former, fluid flows only parallel with the stream and the velocity profile is time invariant at all points, while the latter exhibits distinctly random motion in space as well as time. The instrumental factors are fluid viscous and inertial forces, the ratio of both defines the *Reynolds* number *Re*.

$$Re = \frac{\rho u^2}{L}\frac{L^2}{\eta u} = \frac{\rho u L}{\eta} \tag{2.37}$$

L can again be interpreted as hydraulic diameter or the size of a spherical object in a fluid stream, ρ is the fluid density and η the dynamic viscosity.

Alternatively, *Re* can be deduced as the ratio of diffusive ($\tau_\mathrm{D} = \mathrm{L}^2\rho/\eta$) and convective ($\tau_\mathrm{C} = \mathrm{L/u}$) time scales, yielding:

$$Re = \frac{\tau_D}{\tau_C} = \frac{L^2\rho}{\eta}\frac{u}{L} = \frac{\rho u L}{\eta} \tag{2.38}$$

At low *Re*, viscous effects propagate faster than the fluid flow itself.

The transition between laminar and turbulent flow is thought to occur around $Re = 2000$, which is appropriate in most circumstances. Some experiments hint at turbulence starting at *Re* as low as 400 under certain circumstances [PS13]. In the case of aqueous solutions in a microfluidic context, laminar flow is predominant due to the combination of small channel dimensions and low fluid velocities.

2.1.2.4 Bond Number

The *Bond* number is an important metric to determine the role interface (liquid surface under gas or between two immiscible liquids) tension plays in a given problem. Representing the ratio between gravity and interfacial tension, the *Bond* number *Bo* is defined as

$$Bo = \frac{\Delta\rho\, g L^2}{T_S} \tag{2.39}$$

where $\Delta\rho$ denotes the difference in density between fluids, g is the gravitational acceleration and T_S the surface or interface tension. An appropriate L would again be the hydraulic diameter D_H of a capillary or the contact radius of a droplet. At $Bo << 1$, configuration is dominated by surface effects, with implications for e.g. the shape of a small water droplet on a flat surface, which will assume a hemispherical geometry. By contrast, a large drop, corresponding with a high *Bo* value, will appear flat like a disk.

2.1.2.5 Capillary Number

When interface tension plays a role in microfluidic systems, the *Capillary* number *Ca* indicates the propensity of a fluid flow to break into a stream of droplets below a critical threshold between 0.1 and 0.01. It is defined as the ratio between shear stress $\eta u/L$ and capillary force T_S/L, yielding

$$Ca = \frac{\eta u}{T_S} \tag{2.40}$$

with the characteristic velocity u denoting the rate of shear in a constriction or the rate of buoyant emergence of one immiscible liquid through another [PS13].

2.1.2.6 Weber Number

We is relevant for thin films and jets of fluid. It is derived from the ratio of dynamic (ρu^2) and capillary pressure T_S/L, where u is the velocity of flow and L again D_H, e.g. the nozzle diameter.

$$We = \frac{\rho u^2 L}{T_S} \tag{2.41}$$

A low value of *We* indicates dominant surface tension, typically confirmed by observation of spherical droplets, while inertial forces at high values result in more irregular shaped droplets [PS13].

2.1.2.7 Prandtl Number

In cases where thermal aspects may play a role, the *Prandtl* number Pr indicates whether differences in temperature within the fluid are likely to persist. It is in effect the ratio between thermal and velocity boundary layers and calculated as

$$Pr = \frac{\eta C_p}{\lambda} \tag{2.42}$$

with $\eta, \mathrm{C_p}$ and λ being dynamic viscosity, specific heat capacity at constant pressure and thermal conductivity of the fluid, respectively. A low value ($Pr << 1$) means thermal diffusion is quick compared to convection [PS13] of heat generated e.g. by *Joule* heating in electrophoresis or concentrated light.

2.1.3 Parameter Evaluation

Examining these dimensionless parameters provides insight into system behavior by revealing the dominant physical mechanisms in play without the need for detailed analysis. Through this simplification, similarities between different problems can be identified with greater ease, often correlating a range of a dimensionless parameter to a physical regime (e.g. laminar or turbulent flow, Section 2.1.2.3). Such a generalized treatment of a problem is especially helpful in quickly determining the basic aspects of a design, as shown in Section 3.1. In the case of the devices discussed in this work, the validity of continuum modeling and a laminar rather than turbulent flow regime are considered essential, setting constraints regarding the size of channel features. In practice, many of these constraints are masked by more stringent design rules for manufacturing and the size of target particles.

2.1.4 Dielectrophoretic Effects

Dielectrophoresis, as originally defined by *Pohl* [Poh51] [Jon95] is the induced motion of a polarizable particle within an inhomogeneous electric field. The force involved can be calculated with polarizability $\mathbf{p}$ from Eq. 2.43

$$\mathbf{p} = 4\pi R_p^3 \underline{\epsilon_f} \underbrace{\left(\frac{\underline{\epsilon_p} - \underline{\epsilon_f}}{\underline{\epsilon_p} + 2\underline{\epsilon_f}} \right)}_{\underline{CM}} \mathbf{E} \tag{2.43}$$

as

$$\mathbf{F}_{DEP} = \mathbf{p} \cdot \nabla \mathbf{E} \tag{2.44}$$

where the complex *Clausius-Mossotti* Factor CM determines the sign. Since the driving current used in this work is DC, it is advantageous to rewrite Eq. 2.43 by simplifying the complex permittivity $\underline{\epsilon} = \epsilon + \mathrm{i}\frac{\sigma}{\omega}$ [Pet10], to suit the case $\omega = 0$, yielding

$$\mathbf{F}_{DEP} = 2\pi R_p^3 \epsilon_f \left(\frac{\sigma_p - \sigma_f}{\sigma_p + 2\sigma_f} \right) \nabla(E^2) \tag{2.45}$$

This result reveals that the denominator of Eq. 2.45 will always be negative in all systems where fluid conductivity is higher than that of the particle, indicating repulsion away from areas of higher towards those of lower field strength.

3 Materials and Methods

For the purpose of cell concentration, a continuous mode of operation is chosen at the outset, which allows for increasing the amount of captured cells with runtime, thereby accommodating samples of varying volume and cell counts. In the interest of simplicity, fluid and cell manipulation are designed to be performed without any external fluidic modules, utilizing electro-osmotic flow (EOF) combined with direct current (DC) electrophoresis (EP) based cell movement, both driven by the same externally applied voltage. Target cells accumulate within a gradually tapered constriction whose tip is surrounded by a cavity filled with buffer fluid to provide undisturbed inflow. Within that nozzle, drag due to fluid velocity is expected to exceed the electrophoretic force as a result of the transition from EOF plug flow to a narrower cross section and the resulting pressure differential. Compared to many existing devices employing a constriction (e.g. [CZH+10]), a shallow slope is used to keep shear stress at a minimum and create a region with increasing flow velocities towards the tip of the nozzle. This concept is expected to facilitate the adjustment of EOF through electrolyte concentration in the buffer fluid by giving visible feedback via the position of accumulated cells and perhaps allow the observation of particles with different properties as separate bands. Once the basic geometry is established, characteristic parameters (Section 2.1.2) can be used to determine the viability of the concept and incorporate changes if needed (Section 3.1).

The counter-flow concept is incorporated into a geometry compatible with the design rules in Section 3.3 for dry film resist (DFR, Section 3.3.2). Once verified by simulation using estimated cell and EOF parameters (Section 3.2), several designs based on that principle have been constructed using the *AutoCAD 2014* design suite [Aut14], to produce flexible photo masks for variants using DFR with hydrogel barriers (Section 3.3.2.1) and inverted versions to produce silicone molds (PDMS, Section 3.3.1). With the exception of top slide perforation photo masks for fluid reservoirs, for which an inkjet print suffices, all photo

masks were ordered from *Zitzmann GmbH.* [Zit14]. Offering a resolution up to 64 kdpi, they are suitable for even the smallest channel structures in the µm range.

3.1 Validation of Concept

The first consideration has to be choosing the correct modeling philosophy, which is in all likelihood continuum based, but evaluation of the *Knudsen* number (Section 2.1.2.1) provides certainty. Using the hydraulic diameter D_H as characteristic length, with a channel height of 24 µm and a minimal width of 20 µm, yields 22 µm. At atmospheric pressure of 100 kPa and a room temperature of 300 K, *Kn* results in

$$Kn = \frac{1.38 \cdot 10^{-23}\,\mathrm{J/K}\ 300\,\mathrm{K}}{\sqrt{2}\pi\ 10^{5}\,\mathrm{Pa}\ (2.5 \cdot 10^{-10}\,\mathrm{m})^2\ 22 \cdot 10^{-6}\,\mathrm{m}} = 6.78 \cdot 10^{-3} \tag{3.1}$$

showing the validity of continuum modeling, with very little boundary slip expected (compare Table 2.6).

Another vitally important prerequisite for a functioning design is laminar flow of the medium, indicated by the *Reynolds* number *Re* (Section 2.1.2.3). For water, density is 998 kg/m^3 and viscosity $1.002 \cdot 10^{-3}$ Pa s. Using an estimated fluid velocity of 1 mm/s and again a hydraulic diameter D_H of 22 µm, *Re* is

$$Re = \frac{998\,\mathrm{kg/m^3}\ 10^{-3}\,\mathrm{m/s}\ 22 \cdot 10^{-6}\,\mathrm{/s}}{1.002 \cdot 10^{-3}\,\mathrm{Pa\,s}} = 21.91 \cdot 10^{-3} \tag{3.2}$$

which means that only laminar flow exists. Any buffer solution will have only slightly higher density ρ combined with noticeably increased viscosity η in the case of saccharose containing medium, as shown in Table 3.2, in which case *Re* is even smaller.

During the filling process, the introduction of air bubbles can complicate the use of modules, a phenomenon which can be caused by stream emerging from the nozzle breaking up into droplets [Pet10], the *Capillary* number *Ca* from Section 2.1.2.5 offers an indication how the jet is going to behave. Using the same fluid velocity u of 1 mm/s, a viscosity η of $1.002 \cdot 10^{-3}$ Pa s and a surface tension T_S of $7.275 \cdot 10^{-2}$ N/m

$$Ca = \frac{1.002 \cdot 10^{-3}\,\mathrm{Pa\,s}\ 10^{-3}\,\mathrm{m/s}}{7.275 \cdot 10^{-2}\,\mathrm{N/m}} = 13.77 \cdot 10^{-6} \tag{3.3}$$

indicating a tendency of the jet emerging at the nozzle to form droplets, at least when external pressure (suction) has to be applied.

Buffer reservoirs are sized 3 to 5 mm in diameter and their depth varies little if any within a given module, preventing differences in height from causing undesired pressure driven flow. On the other hand, surface tension may have an effect, especially when the reservoirs are filled until liquid is protruding slightly above them, revealing the typical drop shape. In that case, the comparison becomes very similar to one of two droplets on a surface connected by a microchannel, with the liquid portions below the surface forming part of the connecting channel. This problem calls for the examination of the *Bond* number *Bo* (Section 2.1.2.4), in the case of droplets with radii ranging from 1.5 mm to 2.5 mm. Eq. 3.4 yields

$$Bo = \frac{1054\,\mathrm{kg/m^3}\ 9.81\,\mathrm{m/s^2}\ (2.5 \cdot 10^{-3}\,\mathrm{m})^2}{7.275 \cdot 10^{-2}\,\mathrm{N/m}} = 0.888 \tag{3.4}$$

for the larger and 0.32 for the smaller type of reservoir. Both remain within one order of magnitude of 1, indicating predominance of gravitational effects. Nominally the density of air and pure water are 1.2 kg/m^3 and 998 kg/m^3, respectively, but additives like saccharose slightly boost fluid density, to 1055 kg/m^3 at 14wt%, the difference between densities $\Delta\rho$ is rounded to 1054 kg/m^3. This consideration is important for minimizing the pressure differences between reservoirs by adjustment of fluid level alone rather than having to take droplet geometry into account.

Concerning the mobility of cells in suspension, the *Peclet* number (Section 2.1.2.2) can offer some insight. The minimum hydraulic diameter within the nozzle is 22 µm and minimum cell size is expected to be 0.5 µm. At a temperature of 300 K, the diffusion coefficient is therefore:

$$D = \frac{1.38 \cdot 10^{-23}\,\mathrm{J/K}\ 300\,\mathrm{K}}{3\pi\ 1.002 \cdot 10^{-3}\,\mathrm{Pa\,s}\ 5 \cdot 10^{-7}\,\mathrm{m}} = 877 \cdot 10^{-15}\,\mathrm{m^2/s} \tag{3.5}$$

with *Pe* calculated as,

$$Pe = \frac{10^{-3}\,\mathrm{m/s}\ 22 \cdot 10^{-6}\,\mathrm{m}}{877 \cdot 10^{-15}\,\mathrm{m^2/s}} = 25.1 \cdot 10^3 \tag{3.6}$$

which is above the threshold of 1000 for diffusive mixing, which will not play a role in this device.

3.2 Simulation

The program suite used is *COMSOL Multiphysics 4.4* [COM14], of which two software modules are needed, namely *Laminar Flow* and *Electric Currents*. Boundary settings and material properties are shown in Table 3.1.

Boundary Settings

inlet	zero pressure
outlet	zero pressure
top & bottom	electro-osmotic velocity
channel contours and nozzle	no slip
cathode	ground
anode	variable voltage

Material properties

Parameter	Symbol	Value
fluid permittivity	ϵ_f	$78\,\epsilon_0$
fluid conductivity	σ_f	$60 \cdot 10^{-3}\,\mathrm{S/m}$
resist permittivity	ϵ_m	$3\,\epsilon_0$
substrate conductivity	σ_f	$10^{-12}\,\mathrm{S/m}$

Table 3.1: Simulation Settings

Layout Considerations

As briefly described at the beginning of this chapter, target particles are intended to be dynamically suspended in an area of equilibrium, where particle drag against the flow of buffer medium compensates the electrophoretic force (as illustrated in Fig. 3.1). Given equal flow volume within channel and nozzle and considering the plug flow profile [YIB06] of EOF in undisturbed conditions, fluid velocity will rise in a constriction, an effect, which increases with aspect ratio. Furthermore, as long as buffer fluid has a higher conductivity than the target particles, DEP (Section 2.1.4) provides an additional force component towards the funnel base, which counteracts the EP force and contributes to the concentrating mechanism.

Since the device is expected to perform on a broad spectrum of cells, few assumptions are made except an electrophoretic mobility μ in the region of -2 to $-3 \cdot 10^{-8}\,\mathrm{m^2\,V^{-1}\,s^{-1}}$ [PEPH+11] which is expected to be nearly constant at pH values above six [PW97]. The resulting particle velocity is modeled as $\mathbf{v}_{cell} = \mathbf{v}_{fluid} - \mu\mathbf{E}$ and expected to approach

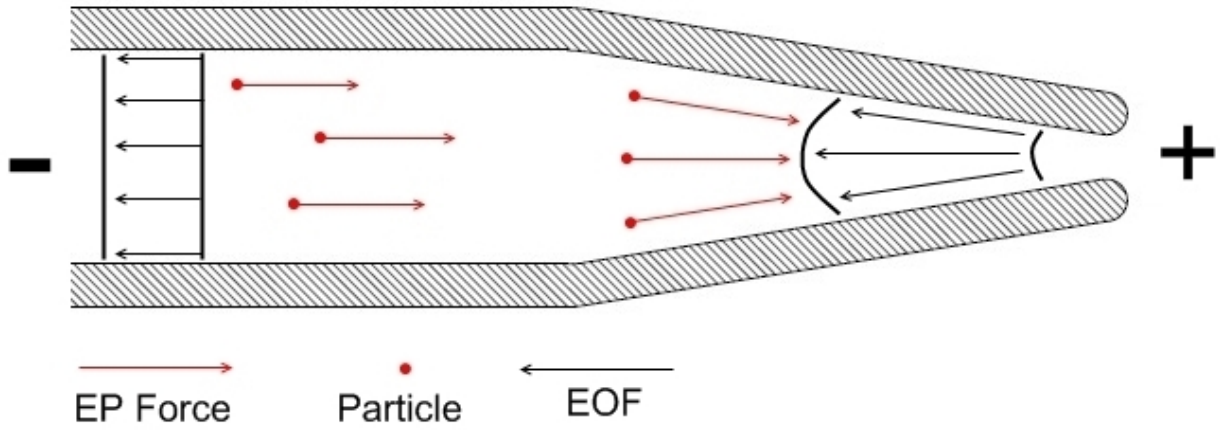

Figure 3.1: EOF flows from anode(+) to cathode(-) while the EP force propels cells towards the anode. Flow velocity will gradually increase from base to tip, stopping the progress of suspended cells within the funnel if the strength of EOF is the correct strength. Electrolyte concentrations can be used to adjust the flow, as described in Section 3.5

zero inside the nozzle, implying accumulation, as seen in a 3D view in Fig. 3.2 and a top view in Fig. 3.3. It is worth noting that a dedicated particle tracing module exists in *COMSOL* v4.4, whose available input parameters are geared towards simulating ionic species in solution and suspended aerosols rather than living cells, which is why a more generic approach is chosen.

Design rules for masks and dry film resist permit features sized 10 µm or more, on top of which a safety margin was observed with the smallest horizontal structures measuring 20 µm. The vertical height was chosen at 24 µm, approximating the thickness of 30 µm dry film resist after development (Section 3.3.2), for which the device geometry was originally designed. Although simulation results prove encouraging, a question mark remains regarding fluid conductivity, which did not affect particle mobility at all in the simulation. Electrolyte concentrations therefore have to be determined experimentally (Section 4.2).

Two gel barrier designs (Section 3.3.2.1) are prepared as an alternative. Hydrogel barriers are electrically very similar to the 98wt% buffer fluid it contains while acting as a solid channel feature, allowing for a reduction in current density and therefore electric field strength within the constriction. The result is a diminished electrophoretic force, while the fluid velocity remains elevated due to the nozzle geometry and EOF along the channel is unaffected. The first variant copies the inverse funnel geometry used in the other designs in PDMS (Section 3.3.1) and DFR (Section 3.3.2) while a simpler model uses a wedge-type geometry, where hydrogel is applied on one side of the channel only as illustrated in Fig. 3.15, which simplifies the application of the gel compared to double sided designs

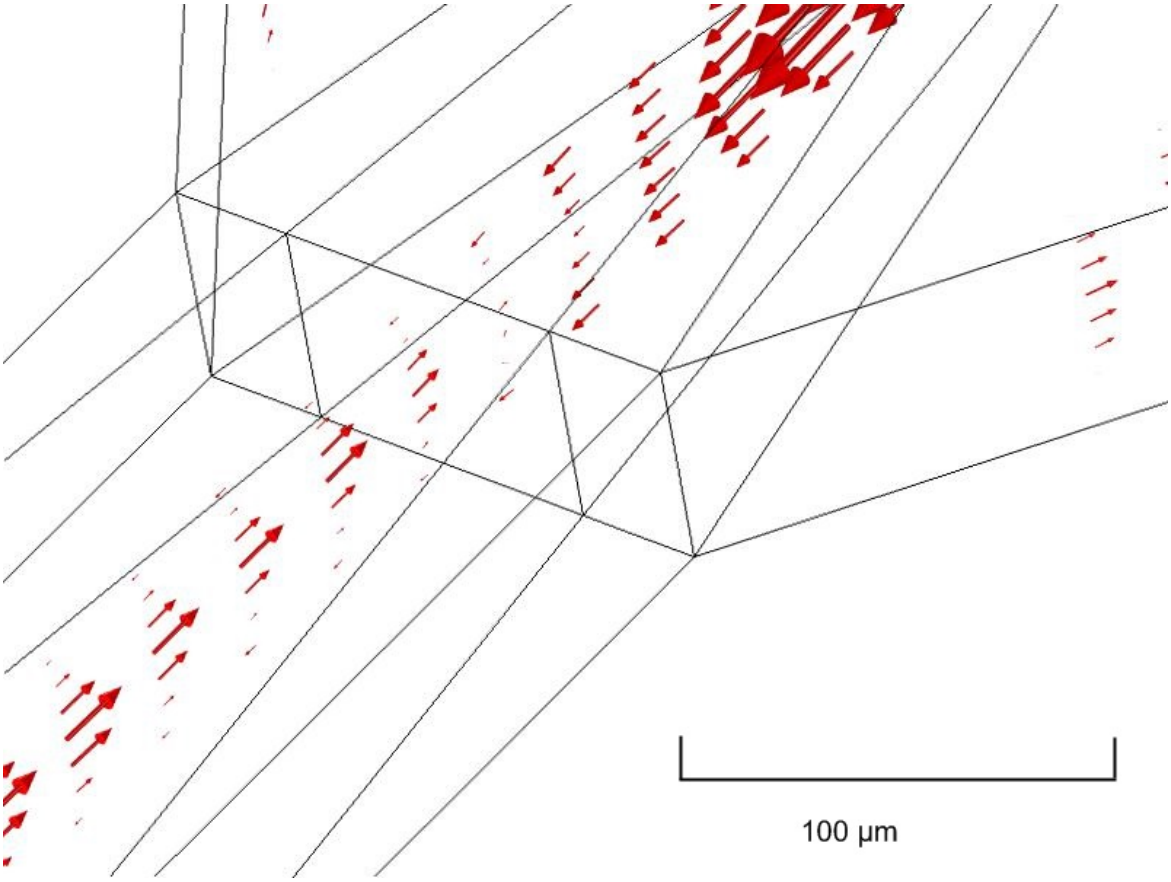

Figure 3.2: The simulated particle velocity distribution shows a stagnant volume at the center upon which the particle velocity vectors converge from both sides. Bottom and top are modeled as glass (substrate, with properties given in Table 3.1), the walls as dry film resist, the effect of which can be seen in a variation of simulated particle velocity with channel height.

by avoiding the need for either separate filling operations on each side or long gel bearing connecting channels. Additionally, a bias towards the base of the wedge was revealed by the simulation result illustrated in Fig. 3.4, where accumulation of particles provides no benefit for sensing, which is best performed in a tight space that can be covered by sensing electrodes. Measuring longitudinal impedance is futile with hydrogel designs, since most of the driving current bypasses the constriction traveling in the gel.

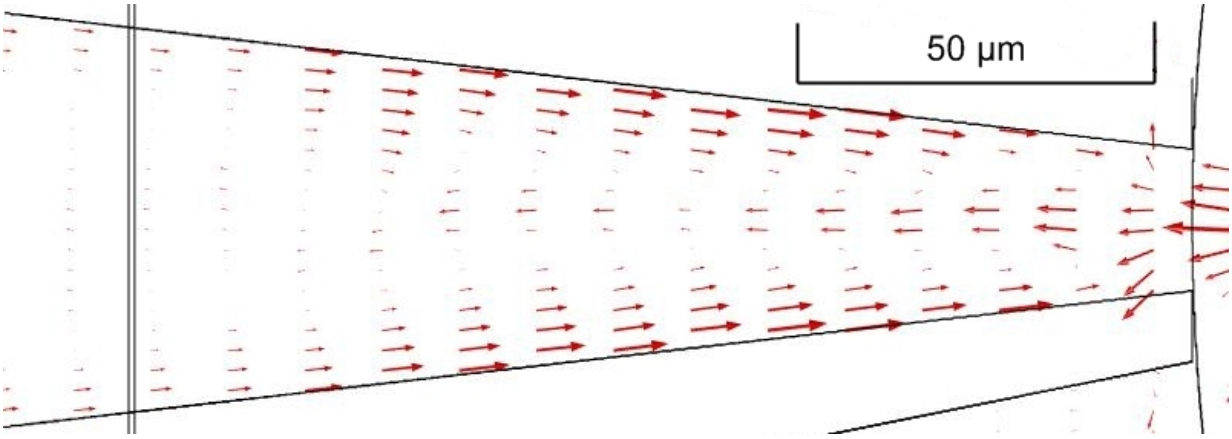

Figure 3.3: Top view of the simulated particle velocity distribution, travel at the tip is limited in one direction and the current in the center diminishes towards the base. Accumulation is supposed to take place where the velocity vectors approach a length of zero.

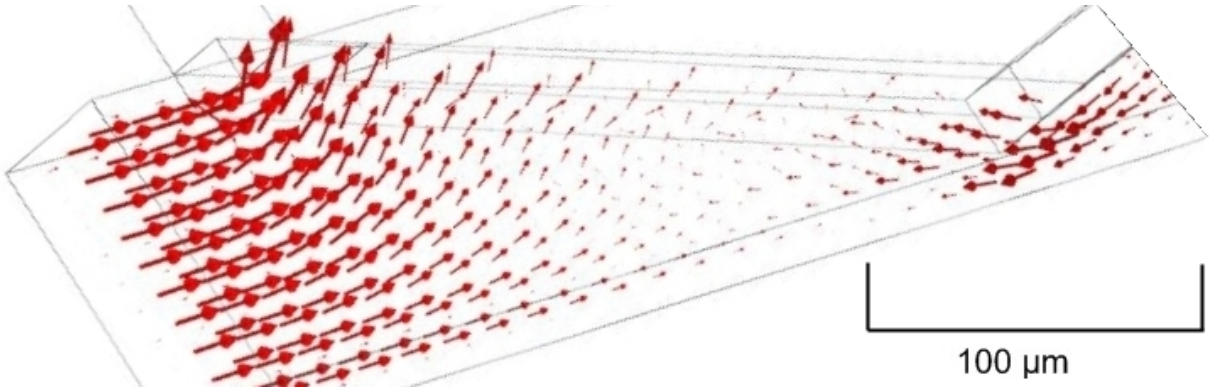

Figure 3.4: Only the lower part facing the cathode (-) side reservoir of the hydrogel wedge on the left side of the channel is shown, since the upper side is not meant to be exposed to particles. The image also reveals a stagnant zone (shortening and disappearing velocity vectors) but also a propensity of cells to lodge into the gel itself at the base of the wedge, which might cause them to stick. The underlying simulation parameters are shown in Table 3.1, where the gel properties are identical to those of the fluid.

3.3 Device Fabrication

While nozzle geometry itself transfers directly to photomasks, care has to be taken to prevent the trapping of air within the structures upon filling, which is realized by the curving of two feed channels around the constriction as seen in Fig. 3.5. Several variants of this basic design are prepared using either two or three feed channels with different lengths and

widths, in order to gain experience and possibly derive improvements. The overall geometry of a compact module is depicted in Fig. 3.6 and one with only two longer channels in Fig. 3.7. Reservoir locations indicated as blue circles can only be approximate in PDMS due to the inherent lack of accuracy of manual punching (Section 3.3.1). Hydrogel (Section 3.3.2.1) barrier designs are also planned, for reasons outlined above (Section 3.2), as well as a simpler, vertically arranged type built around a machined, etched or cut notch in the substrate serving as a constriction.

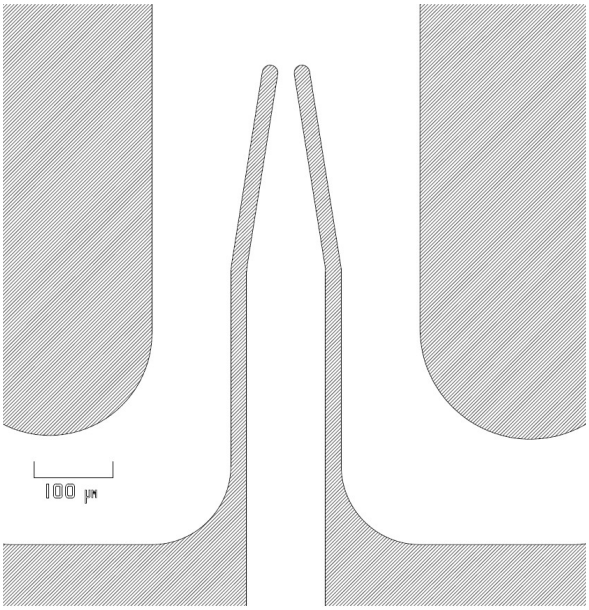

Figure 3.5: A blow-up of the cell concentrating funnel geometry, resist or PDMS shown as hatched areas, the channels themselves are white.

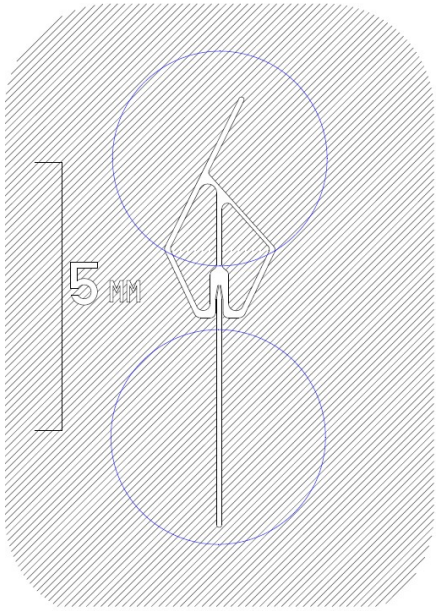

Figure 3.6: Layout of a compact module (PDMS only) the reservoirs shown as blue circles are punched manually, so their location may vary.

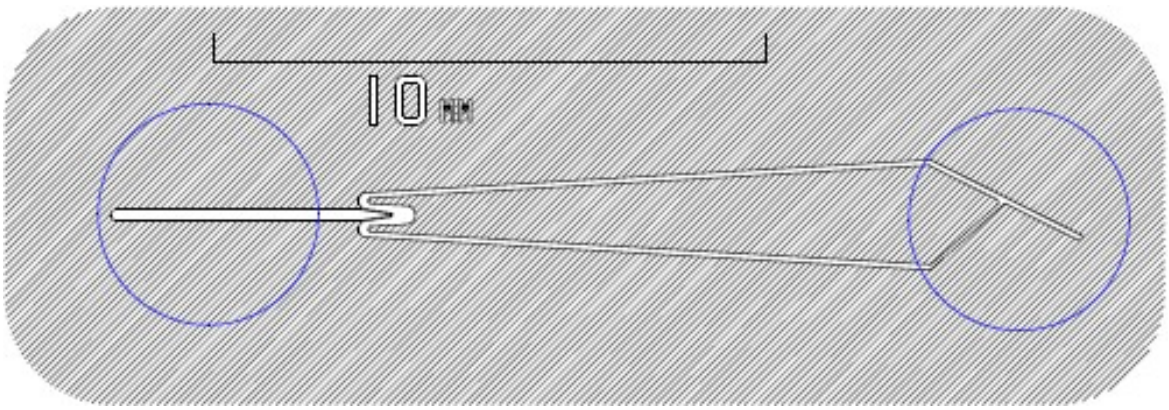

Figure 3.7: The full length module provides better spacing between reservoirs.

Inverted photomasks are prepared in order to produce re-usable silicone (Polydimethylsiloxane, PDMS [Dow14]) molds for all designs except the gel based variants, because hydrogel polymerization requires the absence of oxygen and PDMS is gas permeable. Cast modules provide a much easier route for replacement of spent material without the need for exposing, developing and bonding dry film resist laminated slides for every fresh unit, at the minor inconvenience of introducing more hydrophobic channel surfaces, which complicate the filling process slightly as covered in Section 4.2.1.

3.3.1 PDMS Molding

Inverted channel structures were derived from the DFR designs and used to create molds, using either *SU-8-2000* [Mic14a] or *KMPR 1000* [Mic14b] negative photoresist, which is spin coated onto a wafer (4") or glass plate in thicknesses ranging from 24 to around 100 µm.

Photo Lithography Procedure

1) Application of 4 ml of SU-8 or equivalent *KMPR 1000* onto a cleaned and dry wafer followed by spin coating at 1000 to 4000 rpm for 40 s with a ramp of 10 s, finished by the removal of edge beads if necessary (Fig. 3.8a).

2) Soft bake at 95 °C on a hotplate for 10 min.

3) Expose to UV light in mask aligner (Fig. 3.8b).

4) post exposure bake at 95 °C for 30 min.

5) Removal of unexposed resist using PGMEA solvent and hard bake at 200 °C for 1 h (Fig. 3.8c).

6) After slowly cooling to room temperature, to avoid cracking, the mold is ready for use (Fig. 3.10).

PDMS base (*Sylgard 184* [Dow14]) is blended with one tenth curing agent by weight, poured onto the mold, and optionally de-gassed in a vacuum chamber if time is of essence, otherwise letting it settle on flat surface for several hours will have the same effect. Complete curing can be achieved by exposing the PDMS to a temperature of 70 °C for one hour and once cooled, the modules are ready for use and parts of the silicone layer can be cut out with

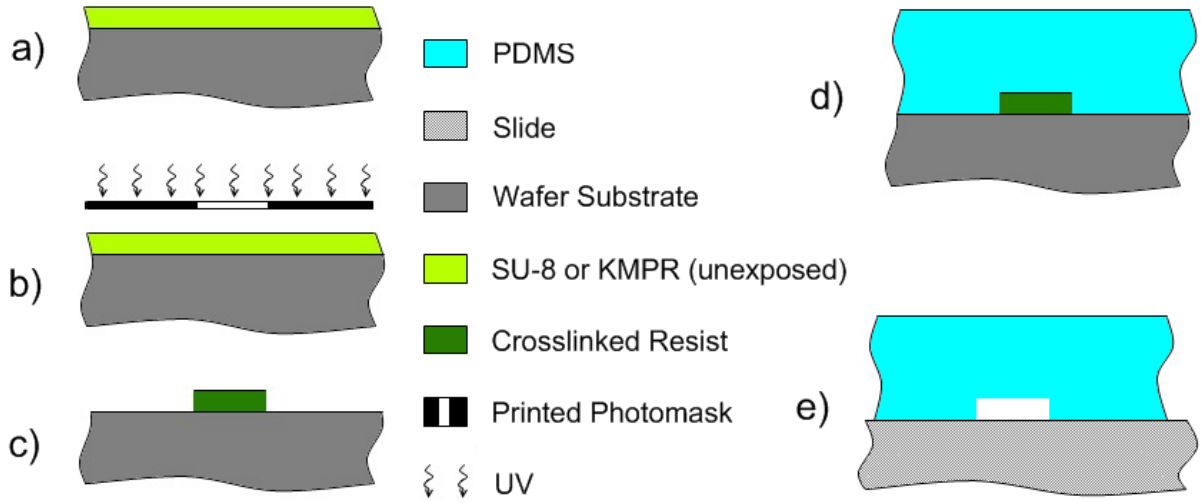

Figure 3.8: Fabrication of a PDMS module. Cross sections at different design steps: a) laminated substrate, b) exposure, c) development, d) PDMS layer poured, e) cured slab of PDMS on a slide - the finished item.

a scalpel and lifted off. Fluid reservoirs are created by punching appropriately sized holes through the channel ends and applying the finished piece of PDMS to a glass slide or polymer sheet. If so desired, silicone slab and glass base plate can be surface activated in an oxygen plasma environment and bonded permanently, preventing leakage at the risk of irreversible clogging, which could otherwise be easily cleared by lifting off and rinsing the slab with isopropyl alcohol.

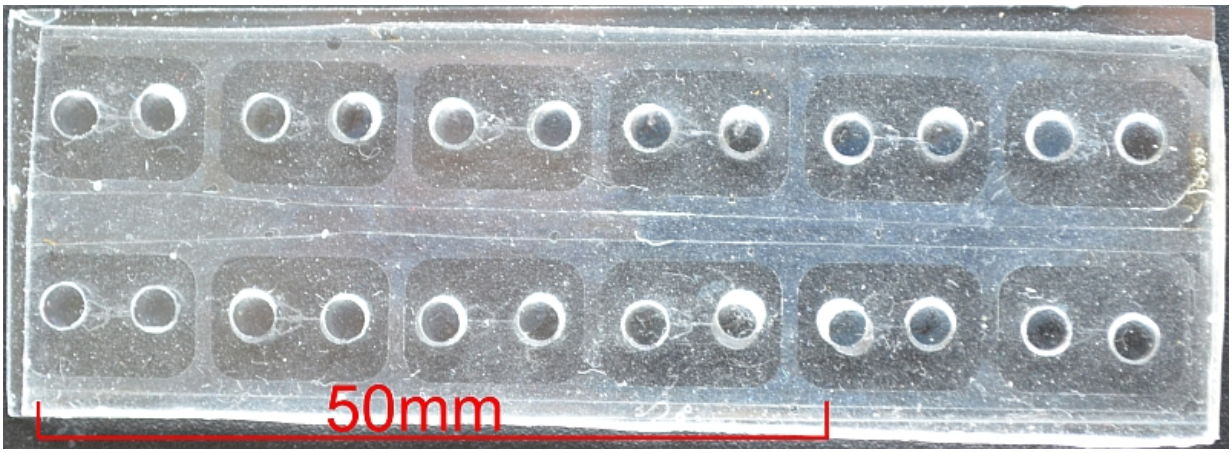

Figure 3.9: An image of finished PDMS modules bonded to a glass slide, an arrangement which makes efficient use of oxygen plasma activation but is less flexible than employing individual units.

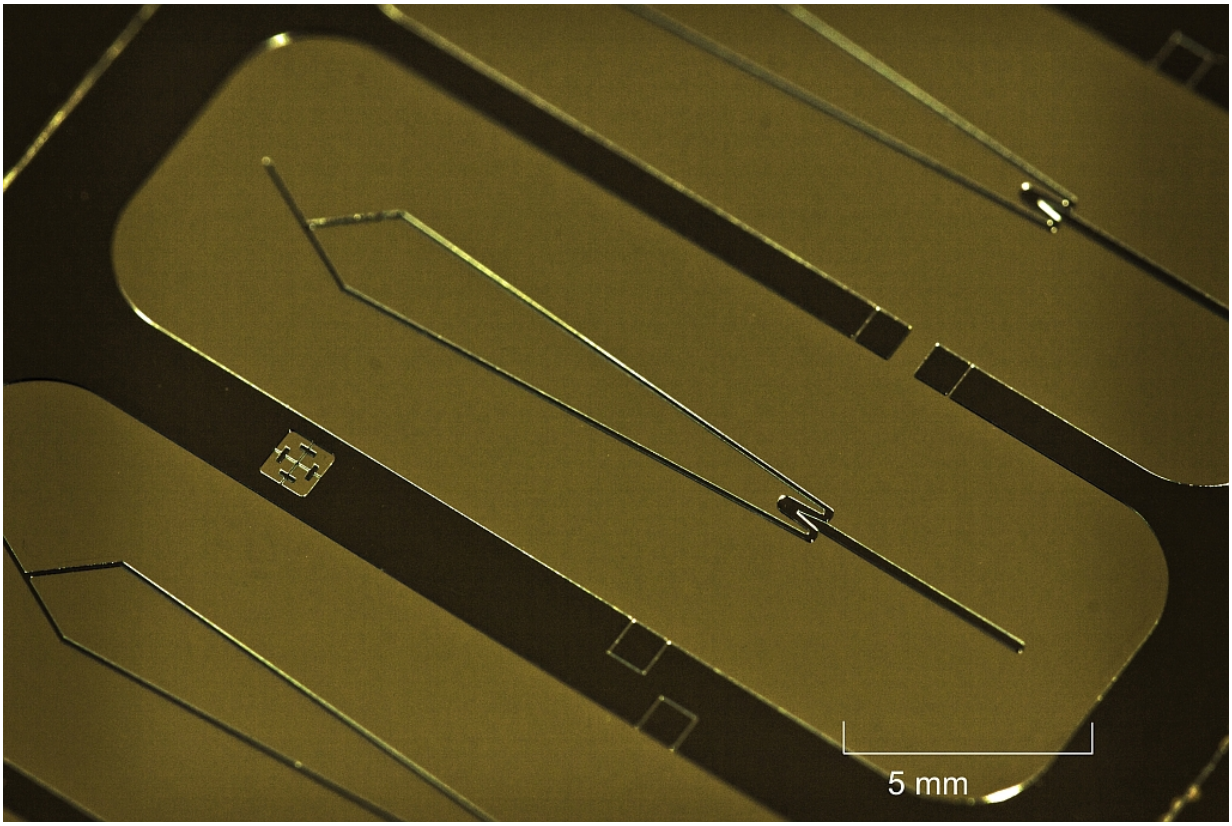

Figure 3.10: A PDMS mold for a full length module fabricated in *SU-8*.

3.3.2 Bonded Slides with Dry Film Resist

The greatest advantage of using a dry film resist (DFR, in this case *Ordyl SY330* [VGA+05]), is ease of application, one pass through a commercial laminating machine at 90 °C is enough to bond it to a clean slide. In order to obtain a smoother surface, a soft bake step for three to five minutes at the same temperature can be introduced, after which the laminated slide is ready for exposure and development. Compared to the environment control and time requirements of spin-coated resists, dry film resist is much quicker, cleaner and more forgiving. These advantages come at a price, though, primarily in the shape of a lower resolution compared to spin resists (Section 3.3.1) and to a lesser degree the risk of cracking slides from the pressure needed to bond the perforated top slide. The available variants measuring 17, 30 and 50 µm thickness shrink by approximately 20% during development, reducing channel depth, but can be coarsely adjusted by stacking layers in additional laminating steps.

Used in a single layer, 30 µm *Ordyl* dry film resist (effectively around 24 µm), which is also reflected in the simulation (Section 3.2), yields the same channel geometry as the PDMS modules, which are based on the same layout, but built using a mold created with an

inverted photomask. More options are available by applying DFR to both sides, additional variations can be introduced by combining one bottom slide with different top slides, which enables the introduction of transitions in channel depth.

The top part is prepared in a separate process by sandblasting, for which *Harke I-XE* [HAR15] dry resist is used, whose resolution is far less important than its elasticity and durability, which even allows it to be re-used multiple times. Perforations are needed for liquid reservoirs and connections to sensing electrodes.

Fabrication of the Perforated Top Slide

1) Laminate a clean slide with coarse, but elastic water soluble *Harke I-XE*, (Fig. 3.11a).
2) Expose the laminated slide for 9 s to UV light in mask aligner using an ink-jet printed mask for liquid reservoirs and access to electrodes in the top slide (Fig. 3.11b).
3) Develop by spraying tap water at low pressure (Fig. 3.11c).
4) Sandblast the reservoir openings using corundum based medium and clean the finished item (Fig. 3.11d), the masks can be peeled off and re-used several times.

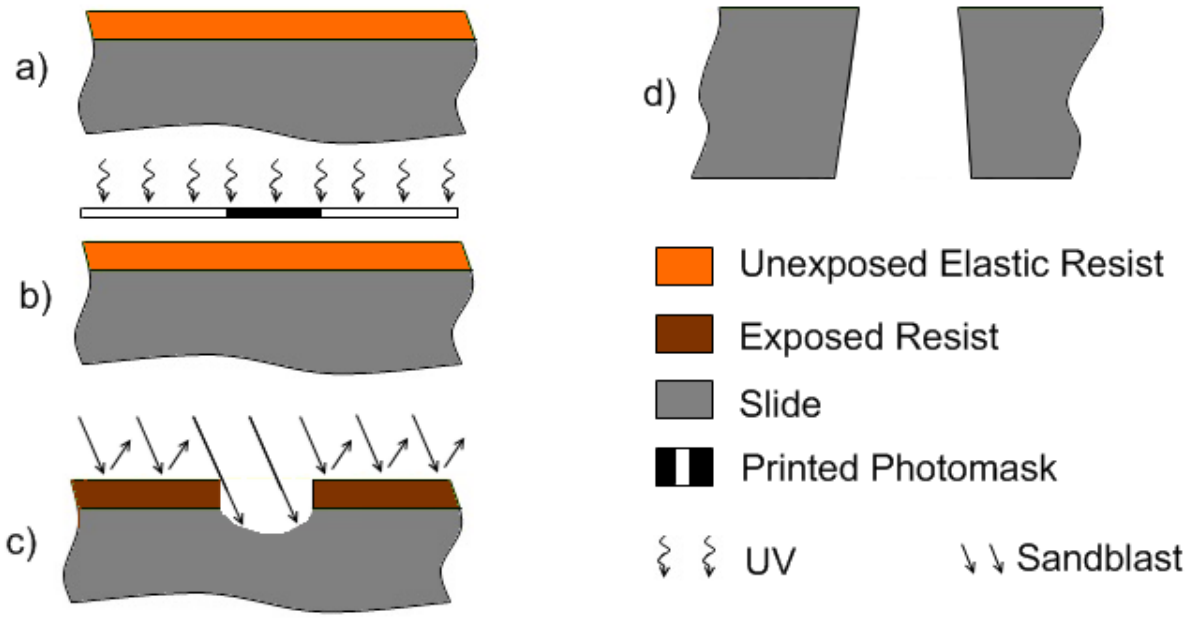

Figure 3.11: Guide to top slide preparation
a) lamination, b) exposure, c) sandblasting, d) complete perforation.

Fabrication of Channel Structures

1) Use a commercial laminating machine to coat a clean, whole glass slide with *Ordyl SY330* resist at 90 °C (Fig. 3.12a).

2) Laminate a perforated top slide at 90 °C and take maximum precautions to avoid wrinkling or tearing, using protective paper wrapping and processing only one item at a time to avoid cracking.

3) Soft bake at 85 °C, for three to four minutes on a hotplate.

4) 20 s exposure to UV light in mask aligner for high resolution, aided by vacuum for best mask contact (Fig. 3.12b).

5) Post-bake at 85 °C for 1 min

6) Develop slides in a mixture of 75wt% xylene and 25wt% 2-butoxyethyl acetate followed by rinsing with isopropyl alcohol (Fig. 3.12c).

7) Align top and bottom features under a microscope, using alignment markers built into the design.

8) Maintaining pressure to avoid movement, move slides to a hotplate at 90 °C and hold them in place for 30 s.

9) Apply 2 kN and 130 °C using a temperature controlled press (Fig. 3.12d).

3.3.2.1 Employing Hydrogel Barriers

The primary feature of gel based barriers is their similarity to the working fluid, providing rigid geometry without also pinching the current (Fig. 3.4), at the cost of more complicated manufacturing. Because the liquid gel has to be introduced by capillary forces, a vertical half-channel-height barrier (called phase guide, [PEPH+11]) is positioned at the desired perimeter location to restrict gel spread (Fig. 3.14). During operation, increased stickiness compared to dry film resist or PDMS may cause cells to embed within the gel with accompanying loss of sample which may pose a problem especially at low cell concentrations.

Two hydrogel materials were tried, agarose at 1wt% to 2wt% in buffer solution (as outlined in Section 3.5) and UV light curable polyethyleneglycol diacrylate (PEG) at 25wt% with

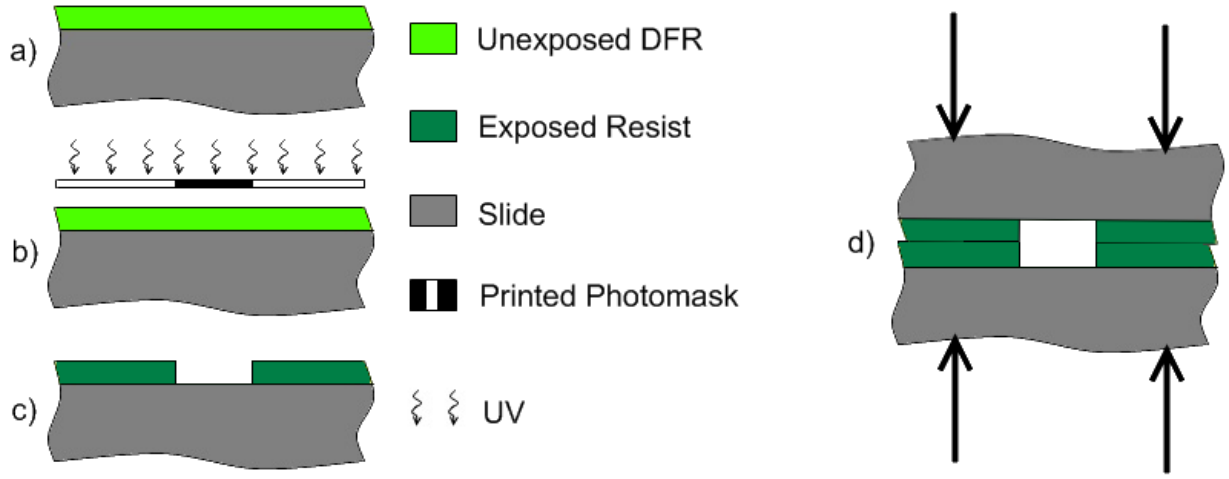

Figure 3.12: Application of Dry Film Resist
a) lamination, b) exposure, c) development in chemical bath, d) alignment and bonding of bottom and top halves under pressure.

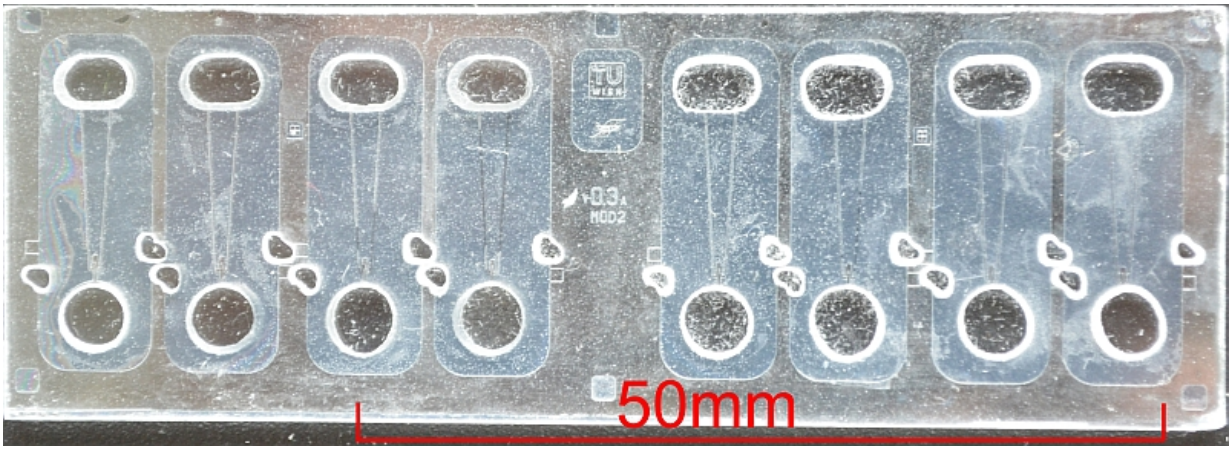

Figure 3.13: An image of a finished set of DFR based modules. The small L-shaped perforations are meant to allow the connection of sensing electrodes but remain unused here.

0.5wt% to 1.5wt% 2-hydroxy-2-methylpropiophenone (HMPP) as photo initiator. The viscosity of the gel increases with concentration, which can therefore be adjusted to suit the application, e.g. to allow for capillary filling while preventing the liquid gel from passing the phase guide. The simplicity of agarose use is offset by its limited time in storage, whereas liquid PEG can be stored for extended periods of time in a UV proof container and once solidified in finished modules, it can be stored indefinitely.

To illustrate the use of hydrogel, the bottom half of the simplest gel based variant is depicted in Fig. 3.15. The phase guide separating fluid (white) and gel (blue) is simply omitted in the top half. A symmetric gel design incorporating the nozzle geometry of the DFR and PDMS variants (Section 3.3) was drawn but considered to be high risk from

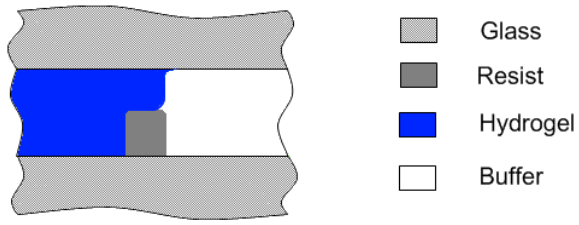

Figure 3.14: Illustration of a phase guide limiting gel spread.

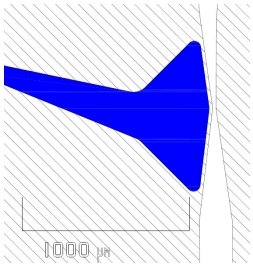

Figure 3.15: A top view of the simpler hydrogel design.

the start, because of the long phase guides involved, which are susceptible to variations in height, as well as gel feed channels having to loop around the cathode side reservoir with a total length of several mm. Both of these aspects place a premium on module quality because a single fault in the gel bearing structures is enough to render the module inoperative.

3.4 Impedance Sensing

A pair of separate surface vapor deposited electrodes is meant to enable electric impedance spectroscopy (EIS [SM10]) on suspended cells. Thin wire leads are connected by soldering and glued in place to prevent mechanical stress on the contact points. A high frequency excitation voltage can be supplied using a frequency generator, the resulting current is then processed by an integrated circuit amplifier into a low output voltage for read-out (Appendix, Fig. B3). This setup helps keeping the leads short, preserving the return signal, which is then recorded by a *Pico Technology ADC-20* [Pic14] data logger.

Surface Deposition of Sensing Electrodes

1) Spin coat a prepared slide or clamped down foil with image reversal (IR) photoresist *AZ 5214E* [Cla14] at 2000 rpm (Fig. 3.16a).

2) Pre-bake the coated module at 107 °C for 5 min (Fig. 3.16b).

3) Expose to UV light in mask aligner (Fig. 3.16c).

4) Reversal-bake at 120 °C for 2 min, which must be controlled tightly to around 1 °C Fig. 3.16e.

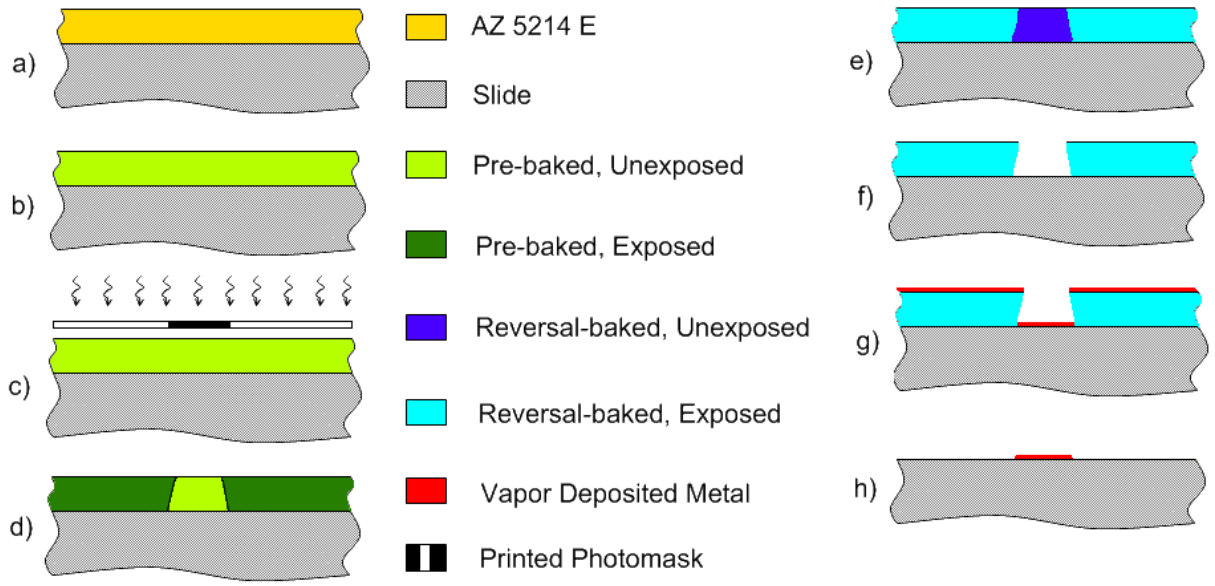

Figure 3.16: Deposition of sensing electrodes.

6) Development of photo resist by immersion, rinsing and drying (Fig. 3.16f).

7) Vapor deposition of 300 nm Au or Pt on top of a 50 nm Ti adhesive layer (Fig. 3.16g).

8) Lift-off in an acetone bath for several hours, followed by the removal of detached metal coating with a soft brush, then rinse and dry (Fig. 3.16h).

Driving voltages acting on electrodes exposed buffer fluid cause electrolysis accompanied by disruptive bubble formation, therefore an effective insulation coating is needed. Possible materials include dry film resist, spin resist, spun-on polyimide (*Kapton*) and polyimide foil of 25 µm thickness with vapor deposited electrodes on the back.

Another approach remains, namely measuring the longitudinal channel voltage at a constant electrophoretic current. With cell walls acting as insulators to direct current, a high concentration of suspended cells within the channel results in a discernible rise in applied voltage, which can be correlated with either a direct cell count by optical means for control purposes or comparing the visible area of the accumulated particles in pixels on identically sized images. For this purpose, the targets are marked in black (R0, G0, B0) and the number of pixels determined via histogram (Section 3.6.2). Since the *HVS-448* features a logging function, recording time, voltage and current, no additional hardware is needed for the task. The principal disadvantage of this method is its inherent lack of selectivity, any insulating particle with the correct electrophoretic mobility will accumulate and cause a rise in (DC) voltage.

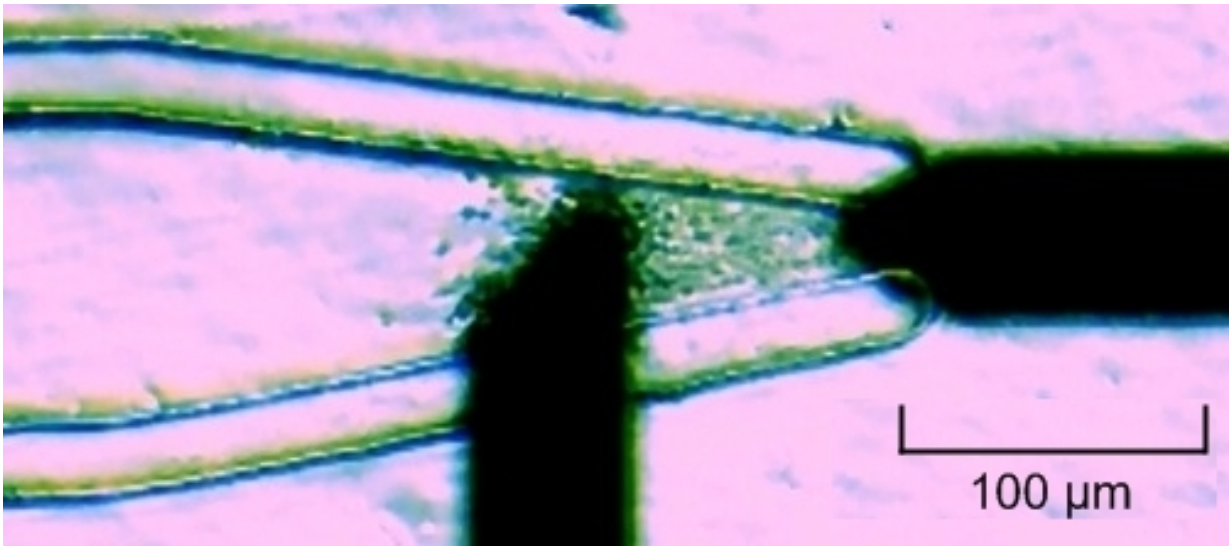

Figure 3.17: A close view of the sensing electrode tips, with concentrated cells.

3.5 Buffer and Sample Preparation

All operating fluid described here is based on sodium tetraborate, which features better electrical properties than alternatives like EDTA, with decreased joule heating and can be used over a wide range of concentrations [BK04]. To ensure cell viability, the pH value should not exceed 8.5 [PEPH$^+$11], so the concentrated electrolyte (chosen at 100 mMol/l) used for blending of working fluid, is adjusted slightly below this value by buffering with boric acid. This ensures pH of the final product remains between 7 and 8.5, which keeps the cells alive for at least several hours, while maintaining a relatively constant surface charge and therefore, consistent electrophoretic mobility [PW97]. To keep the buffer clean, batches of a few ml of working fluid are blended daily with de-ionized water as a precaution, which avoids potential contamination from repeated handling. Additives (percentages by weight) like 14wt% saccharose can be used to increase the fluid density, helping to keep cells with a tendency to sediment suspended or methyl cellulose at 0.1wt%, which is supposed to match EOF on glass and PDMS surfaces. Alternatively, PDMS structures can be immersed in a 5wt% solution of polyvinyl alcohol (PVA, *Mowiol* [Sig14]) for an hour to alter its surface properties and approach the surface chemistry of glass, without the need for additives in the working fluid itself.

Saccharomyces cervisiae (baker's yeast) and *Escherichia coli* samples are extracted from culture via inoculation loop, suspended in 1 ml freshly blended buffer solution in a vial and vortex stirred for at least half a minute to dissolve any cell clusters. A *Neubauer Chamber* [Cel14] is used to determine particle density, always preceded by at least one 1

Working Fluid Comparison		
	density [kg/m^3]	viscosity [Pa s]
	ρ	η
with 14wt% saccharose	1.055	$1.534 \cdot 10^{-3}$
H_2O	0.998	$1.002 \cdot 10^{-3}$

Table 3.2: Medium Properties

in 10 diluting step to keep the cell count per window within visually discernible limits, see Fig. 3.18. A chamber consists 16 squares holding 4 nl each, which are filled by capillary action after placing a thin glass cover on top and applying several µl onto its edge, counting is then performed visually. Using a microscope mounted camera, a magnification of at least 100 is needed in the case of *E. coli*. With cell density determined, a series of samples at different concentrations can easily be obtained by serial dilution. For improved cell visibility and contrast within the microchannel, cells can be stained with acridine orange (AO), a fluorescent dye. A µl is added to the sample, blended and incubated for 10 min and washed (diluted, centrifuged and decanted) several times with fresh buffer to reduce background fluorescence. Excitation is performed by blue light of 450 to 490 nm wavelength, reflected by a 500 nm dichromatic mirror and passed through a *Nikon B-2A* 515 nm long pass filter.

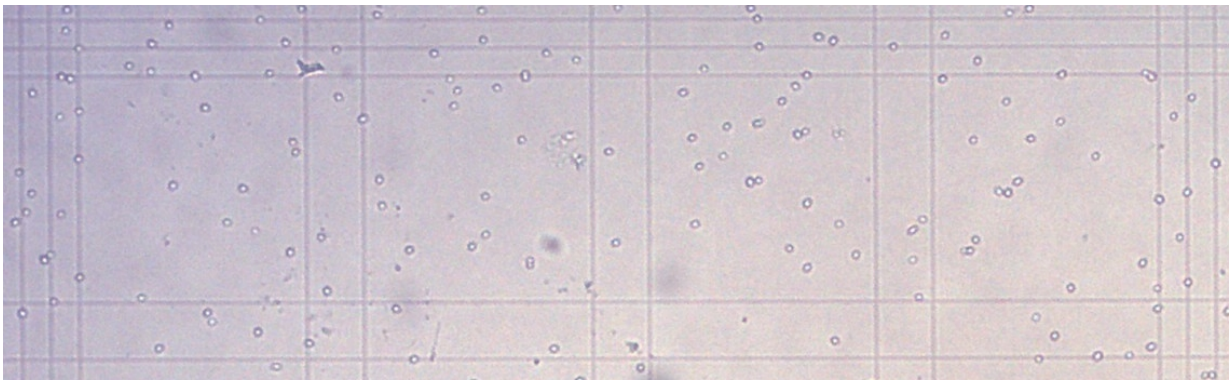

Figure 3.18: Partial view of a *Neubauer Chamber*, each square holds 4 nl, a normal count involves 16 rather than only four squares.

3.6 Experimental Setup

3.6.1 Electrophoresis

The electrophoretic driving voltage is applied via corrosion resistant electrodes, submerged in the reservoirs and connected to a self regulating power supply (*LabSmith HVS-448* [Lab14]), voltage and current settings are available up to (+/-) 3 kV and 62.5 mA, respectively, which are routinely limited to 500 V and 60 µA as a precaution. The power supply is software controlled and connected to a PC via (emulated) serial port.

3.6.2 Read-Out and Compilation

All components along with the buffer fluid ionic concentration and cell sample quality should be tested using a spare module before performing any dedicated measurements, by optical confirmation of basic function. Noting down the amount of fluid dropped into both of the reservoirs helps reliable reproduction.

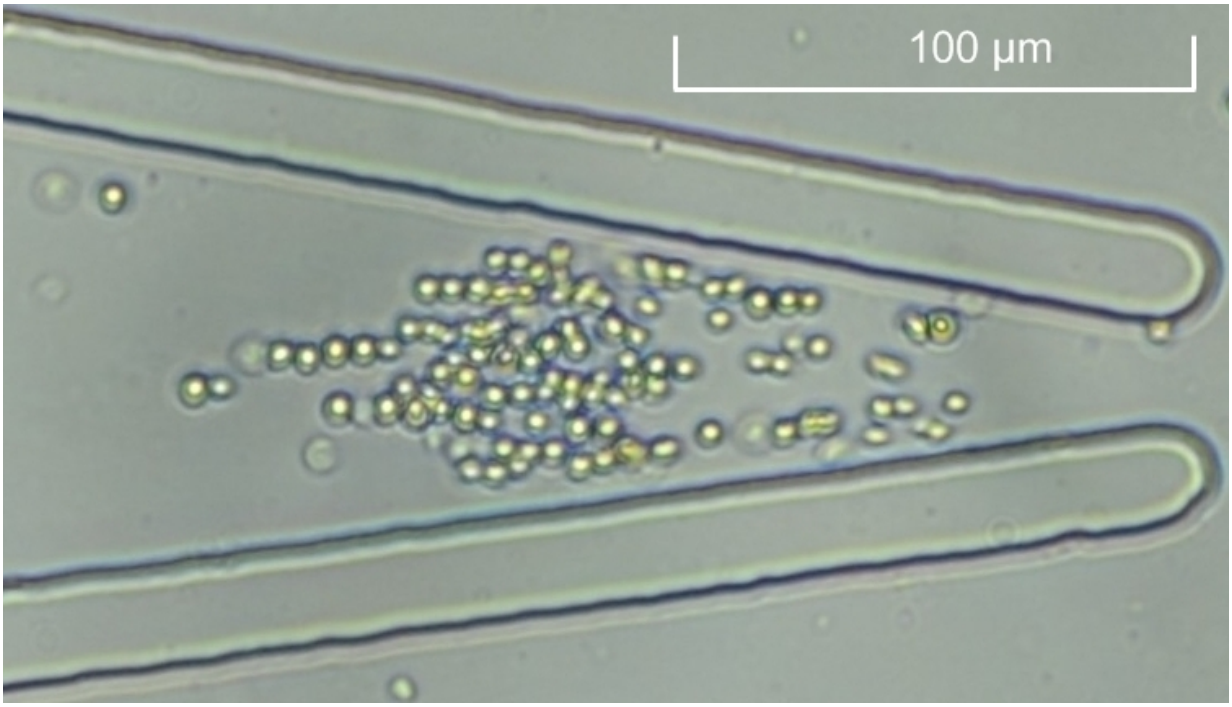

Figure 3.19: Typical screenshot used for cell count of a *S. cervisiae sample*

After the completion of all preparatory steps and inserting the fluid sample, the module has to be aligned under the microscope (using a magnification factor of 100 or greater)

and connected to the power supply. Cell concentration can be observed continually and recorded by a mounted camera, permitting the use of snapshots to perform either a direct cell count (Fig. 3.19) or measure the amount of occlusion by target particles by marking and subsequent determination of the number of pixels via histogram (Fig. 3.20), which can be used as a reference against electric measurements. The power supply trace log and video recording should start before activation of the driving current and stopped only after deactivation, to provide a complete recording.

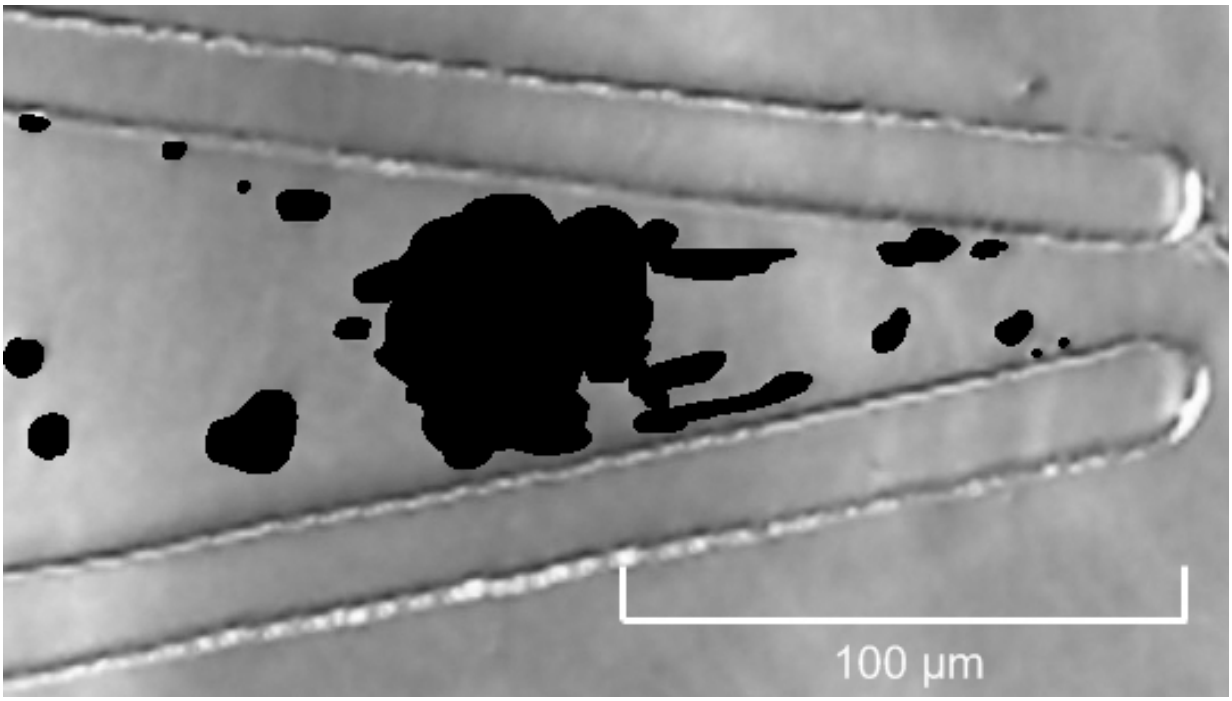

Figure 3.20: Example of an image used for pixel count by histogram

3.6.2.1 Post-Processing

Following the cell or pixel count, trace log data can be copied into a spreadsheet and processed to calculate impedance values at each time step and derive the desired statistical quantities, like median value and average deviation. The reference value used for normalization (V_{min}, Z_{min}) is obtained a the averages from an interval (100 entries long) near the beginning of the trace log, once the power supply output has steadied, but no cells have accumulated yet. The measured maximum values (V_{max}, Z_{max}) are taken in a similar way, but using an interval of the same length that ends where the driving current is turned off. The validity of both can be verified by calculating and comparing the average deviation

within the intervals, which are also used for the calculation of error bars. Graphing the data reveals the correlation between optical and electric measurements as well as their fidelity, which can be seen in the figures shown in Section 4.3.2.

4 Results and Discussion

The different technologies presented in Section 3.3 were evaluated for the fabrication of devices based on several designs whose photo mask prints can be found in Appendix C. The compatibility of the designs with each technology was examined in a series of experiments which are discussed in Section 4.1. The established operation protocols (Section 4.2) and the results of cell concentration experiments (Section 4.3.2) are presented in this chapter.

4.1 Technology Evaluation

Originally, different technologies were intended to complement each other, with PDMS modules (Section 4.1.1) used for calibration of buffer fluid and the bulk of testing, DFR types (Section 4.1.2) used for electronic sensing with the dedicated electrodes (Section 4.3.1) and hydrogel based sub-variants as a parallel pathway and a potential backup option. Because the issues encountered in producing DFR modules could not be solved, PDMS remained the only viable option.

4.1.1 Cast Modules made from PDMS

The spin resists used to create PDMS molds (Section 3.3.1) can be applied in continuously varying thickness allowing to adjust channel depths of the finished module from about 10 to more than 100 µm, although only a few values (24, 38 and 60 µm) were used in practice. PDMS modules of different lengths and depths (Section 3.3) were compared, for which purpose long channeled modules (Fig. 3.7) of 24 µm depth along with compact ones (Fig. 3.6) of 24 and 38 µm, measured by profilometer, were used. At 60 µm, extraction of the PDMS structure proved unreliable and with 110 µm, the finer features could not be

saved at all. When extraction worked, all modules performed flawlessly with proportionally increased driving currents compared to those of shallower modules, however.

In the full length design, cell accumulation could only be observed within a narrow band of driving currents of 2 to 7 µA (Table 4.1). The lower limit is owed to power supply jitter at such low outputs, which manifests in pulsating cell movement, and to residual pressure differences between the reservoirs overcoming the electrophoretic force at the lowest settings. The upper bound, beyond which the majority of cells pass the constriction towards the anode, depends strongly on the combined cross section and length of the feed channels. In testing of the long design with only one feed channel open and the other blocked by air, the maximum usable current was reduced to 4 µA or roughly half of the value recorded with both open, while the same effect could barely be replicated at much higher driving currents of 30 to 40 µA in the compact design with reservoirs spaced as far apart as the padding around the channels permitted. The only downside proved to be module handling due to its small dimensions, and the need to accurately punch through the PDMS slabs to create the reservoirs. Aside from this minor issue, small size is generally an advantage and allows more modules to be made during each casting operation.

A sub-variant (mentioned in Section 3.3) employing a simplified vertical threshold geometry used a notch or groove within the substrate (glass or polymer slide) to establish a connection below a 100 µm wide PDMS barrier as outlined in Fig. C17. Doubling the width of the downstream channel was intended to contribute to the concentrating effect by reducing the fluid velocity beyond the constriction, but proved irrelevant, with some modules performing better in 'reverse'. Functionality could only be achieved using a very tight constriction and proved strongly dependent on driving current, requiring a minimum of 40 µA and nearly 1 kV (Table 4.1) to reliably accumulate cells. Due to the tightness of the constriction, a few modules showed a filtration effect and would permanently trap cells. These issues, coupled with a lack of reproducible positioning of suspended particles and a high incidence of defects made the vertical design unattractive.

4.1.2 Dry Film Resist Modules

Three *Ordyl SY300* dry film resist (Section 3.3.2) variants of the long channeled design (Fig. 3.7) were tested by using different top slides, one with fully symmetric top and bottom features, doubling channel height, one including a vertical step at the nozzle to accentuate the flow speed difference and a one-sided module using the top slide as cover only. By application of multiple layers per slide and using different gauges of DFR (17, 30

and 50 µm), the number of these variations could be expanded. Despite many attempts to improve module quality and precision, especially during the bonding process, the DFR resolution proved too coarse to reliably form uninterrupted barriers and the development process affected the height of the finer structures more than larger areas like contact pads, resulting in profuse leakage within the nozzle (with cells of *S. cervisiae* passing undisturbed) at all thicknesses of DFR in single sided as well as double sided modules, even with optically perfect alignment.

By contrast, hydrogel designs (Section 3.3.2.1) always require a vertical step geometry as a phase guide, so this peculiarity could potentially be exploited for this purpose. In light of the manufacturing problems experienced with the material, only one test of the more complex design was unsuccessfully performed, while several iterations of the simpler variant (shown in Fig. 3.15) were tried with continuous improvements in module quality and different combinations of resist thicknesses and still found uncontrollably leaking hydrogel. Even modules with visually perfect channel features suffered from uneven padding surfaces, which prevented flush bonding and introduced leaks throughout the channels. These gels are incompatible with PDMS, because oxygen diffusion through the gas permeable PDMS prevents complete radical polymerization.

4.1.3 Spin Resist Modules

Liquid spin resist used to create molds (Section 3.3.1) was applied directly to a glass slide and exposed under the photomasks for DFR. This type of use revealed differences between resists, because SU-8 [Mic14a] proved too brittle, which lead to chipping and detached fragments blocking the channel structures as well as leakage, while *KMPR 1000* [Mic14b] remained intact. The resulting module was watertight and functioned properly, even though significant warping could be observed within the geometric features of the constriction from mounting the top plate on partially cured resist. This aspect (unpredictable deformations will prevent alignment of top and bottom parts) effectively precluded the production of a working double sided module. Using a single layer of resist, with the resulting uniform thickness, phase guides for a hydrogel design can only be realized with a double sided module, where channel structures have to match, even though the phase guides themselves are single sided. The KMPR resist module showed an equivalent function and voltage to current relation to the PDMS designs (Table 4.1). An advantage over hydrophobic PDMS is given by capillary priming of the hydrophilic KMPR/glass devices.

4.2 Basic Function

The power supply offers two main operating modes, constant voltage and constant current with their own set of advantages and disadvantages. Voltage driven operation is fail-safe in case of an interruption of the of the current path by an air bubble but, from experience, shows greater fluctuations than constant current mode, even with buffer medium alone, which can only be attributed to the power source regulator. Therefore, the latter is used throughout with voltage used as output signal, with the added benefit of better voltage than current resolution, since channel conductivity is such that a maximum of 200 to 400 V out of voltage range of 3 kV, but only 10 to 20 µA of the available current range of 6.25 mA. In the shallowest modules with channel depths of 24 µm, this corresponds to a maximum current density of 2.08 A/cm^2 and 4.17 A/cm^2, respectively. Sampling time can be adjusted between the default value of 25.6 ms down to below 1 ms, a feature, which after a few tests without visible differences, remained un-used, however.

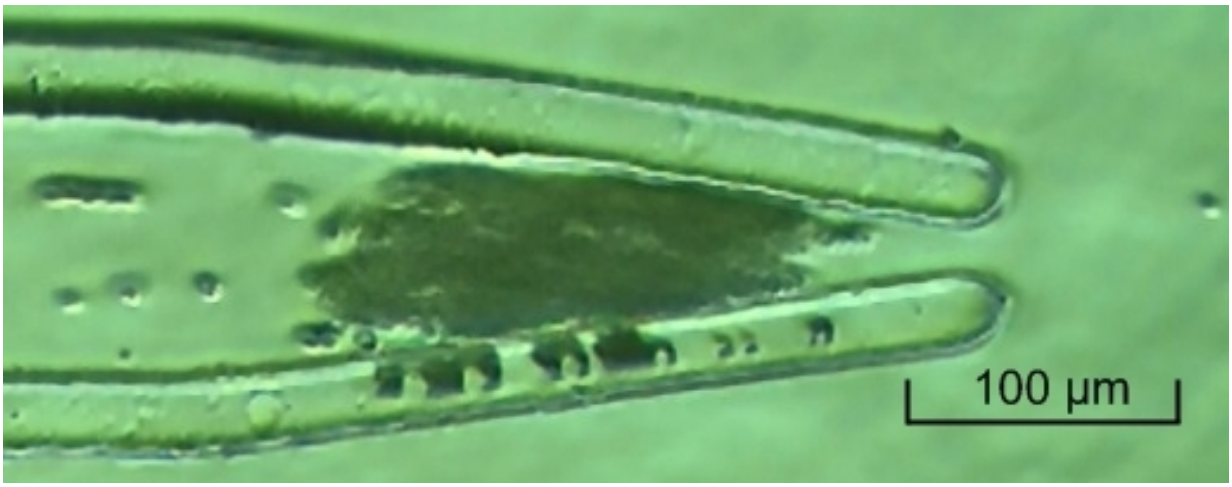

Figure 4.1: Screenshot during the first successful cell concentration test with *S. cervisiae*

Initial testing aimed at establishing the working principle and adjusting parameters, especially electrolyte concentration and driving current. For this purpose, a short channeled PDMS module with a channel depth of 38 µm was used, because of easier cleaning and drying compared to bonded variants with enclosed channels as well as ease of module replacement (Section 3.3.1). Primed and set up as described in Section 3.6, a test was performed with *S. cervisiae* at an electrolyte concentration of 1 mMol/l of sodium tetraborate (Section 3.5), where EOF had proven dominant and cells remained within the cathode side (Fig. 3.1) reservoir. At a concentration of 5 mMol/l, desired functionality was observed under 100x magnification with driving currents between 5 and 12 µA (0.66 A/cm^2

and 1.58 A/cm^2, respectively) yielding the best results. These values represent a compromise between speed of accumulation and steady positioning of the suspended target cells. Measured voltages were 50 to 65 V at the former setting and 120 to 170 V at the latter. The lower and upper bounds of these voltage intervals correspond to clear buffer and a visually observed dense concentration of cells in the nozzle (Fig. 4.1), implying a sensing capability. An issue of cell sedimentation may appear, which can be resolved by using 14wt% saccharose by weight as an additive (Section 3.5), increasing the buffer fluid density to better match that of *S. cervisiae*. Although viscosity is also affected (Table 3.2), the physical differences remained small enough that no visible changes in function were observed in practice.

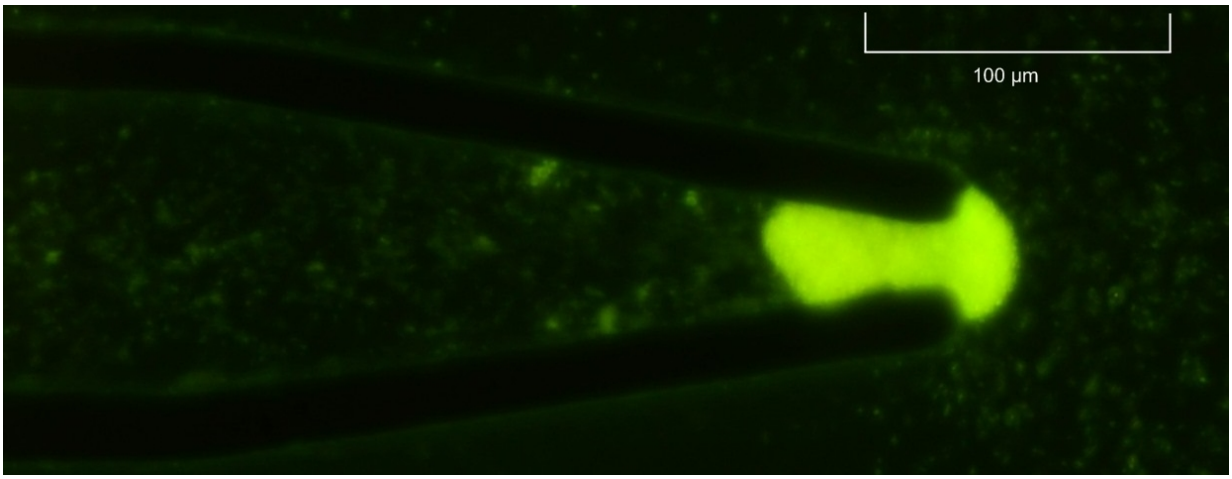

Figure 4.2: Image of acridine orange (AO) stained *E. coli* filling the entire nozzle tip and extending beyond, which is only possible through cohesion.

Testing revealed that single isolated cells were 'overshooting' the constriction and being lost, an issue, which could be strongly reduced by fine tuning the electrolyte to 4 mMol/l of sodium tetraborate, resulting in a measured buffer conductivity of 1770 to 1850 µS/cm at 24 °C. At this value, a driving current of 10 µA applied to a module with 24 µm channels results in a current density of 2.1 A/cm^2 and the corresponding electric field strength is 1.2 kV/cm which is below the lysis threshold of both, *E. coli* and *S. cervisiae* [LT99]. The electrophoretic mobility of both cell types proved very similar, so an electrolyte concentration of 4 mMol/l was kept in both cases and different modules were first tested with the former for easier observation. In an attempt to maximize the density of suspended target cells, several ways to equalize flow velocity profile around the channel circumference were tested: changing the fluid properties through the addition of 0.1wt% of methyl cellulose, which at this concentration approximately equalizes the strength of EOF over PDMS and

glass surfaces, by treating the PDMS modules for an hour in 5wt% polyvinyl alcohol (Section 3.5) and using a polymer slide, i.e. adapting the substrate to PDMS rather than the other way around. Changes to the channel surfaces had the desired effect while adding methyl cellulose to the fluid allowed all target cells to pass the constriction, a phenomenon which was repeated by residues of fluorescent dye (acridine orange, Fig. 4.2) in the buffer. Stained cells have to be washed in at least five cleaning cycles of repeated dilution with de-ionized water, centrifuging and decanting to preserve functionality.

Module	Current [µA]	Voltage [V]
short 24 µm	7	80 - 210
short 38 µm	12	90 - 170
long 24 µm	7	230 - 290
single ch. long 24 µm	4	220 - 250
vertical 24 µm	40	900

Table 4.1: Comparison of the relationship between current and voltage using different modules at an electrolyte concentration of 4 mMol/l and a *S. cervisiae* sample.

Table 4.1 shows the relationship of voltage versus driving current for the PDMS based modules outlined in this subsection, the upper values correspond to a dense concentration of cells in the nozzle.

Under these circumstances, it became clear that:

* Channel length increases the driving voltage at a set current and impairs concentrator function by limiting flow rate and decreases the upper usable limit of the driving current.

* Increased channel depth mitigates the effects of channel length and facilitates priming but reduces sensitivity to cell accumulation due to increased nozzle cross section.

* Increasing the cumulative cross section of the feed by using more and/or wider channels also raises the threshold, but at the same time helps preserve sensitivity.

In addition to living cells, the devices were also tested with polystyrene beads of 4, 8, and 12 µm. With the same buffer concentration of 4 mM, all particles passed the constriction, indicating a higher electrophoretic mobility. Functionality could only be established by using pure de-ionized water instead (1 µl of sample diluted in 1 ml of de-ionized water,

Fig. 4.3), whose low conductivity meant that the voltage cap of 500 V (Section 3.6.1) had to be lifted, since the driving current of 6 µA resulted in a voltage of 910 +/- 20 V. The focus remained on living cells.

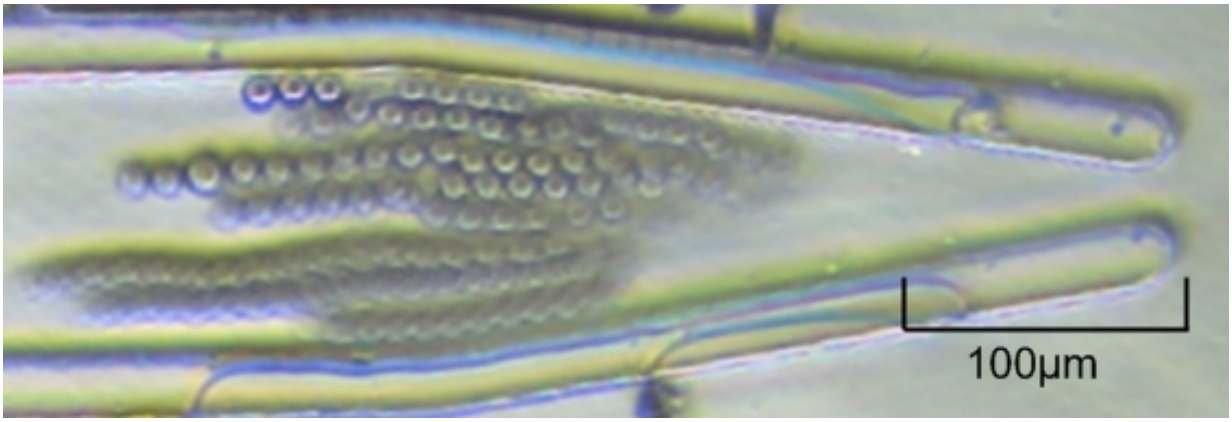

Figure 4.3: A concentration test with polysterene beads with a diameter of 12 µm in de-ionized water.

4.2.1 Priming

The complete module can be primed from the constriction base by filling the cathode side reservoir (Fig. 3.1) with buffer solution and applying suction to the opposite end if required, as is the case of hydrophobic PDMS channels. By contrast, filling from the anode reservoir with its multiple channels (Fig. 3.7 and Fig. 3.6) results in an uneven distribution of fluid and traps bubbles of air. If capillary filling is interrupted at the constriction, it will resume once the medium is forced beyond the threshold and some diligence is needed to keep pressures and therefore fluid velocities low (see Section 3.1), which includes avoiding inducing sudden changes upon release of the suction device. In case small bubbles remain after priming, letting the medium settle for several minutes may be sufficient for them to dissipate, otherwise, flushing is required as pinching or even interruptions in the liquid columns inevitably degrade module function and especially affect impedance measurements.

4.3 Cell concentration and detection experiments

4.3.1 Insulated Sensing Electrodes

With surface electrodes connected as described in Section 3.4, a process which proved reliable in the case of insulated glass slides but problematic with flexible polyimide sheet, where the miniscule weight of the wire itself is enough to tear the contact pads off, the module can be connected to the amplifier (Fig. B3 and Fig. B4). For safety reasons, great care must be taken to first secure all module side contacts with glue and keep the sheet sandwiched between slides to achieve a usable level of surface smoothness, which is required for water tight placement of a PDMS channel structure on top of the sensing electrode pair and even then, clamping is usually needed to provide flush contact and prevent leaks.

Testing quickly indicated critical weaknesses of the insulating coatings, even when applied in multiple layers, they failed after continuous use and triggered both, a constant downwards shift of the peak frequency and an increase in overall sensitivity until breakdown occurred, accompanied by gas bubble formation, at which point, even the lowest driving current setting caused an over voltage warning from the data logger. The time frame for this breakdown varied in the low minute range. As an potential remedy, 100 µF coupling capacitors were employed, to minimize stray DC currents traveling via the amplifier circuit, which were thought to contribute to insulation breakdown, but to no avail. The polyimide sheet proved resistant to electrolysis but ultimately too thick at 25 µm and made the device insensitive even at extremely high cell concentrations. The durability of the polyimide sheet identifies the coating process as the culprit rather than the material itself.

Even though *Picolog* readings were unsteady, a few tests indicated the viability of the approach. Excitation at frequencies of 900 kHz to 1.4 Mhz at voltages between 1 and 10 V (frequency generator maximum voltage) were used, depending on insulation thickness and adjusted to generating output voltages near the maximum of the sensor range, between 2000 and 2500 mV, for best sensitivity. One (expected, due to capacitive coupling) effect was a step in the output voltage, caused by the activation of the EP driving current, which turned out to be 10 to 15 mV or approximately 0.5% to 0.7%. The signal strength alone would not have posed any problems by itself, if the system response had settled in later. As it was, gradual galvanic breakdown resulted in the output voltage creeping up at a slow rate around 10 mV per minute followed by eventual failure of the insulating layer, marked by over voltage even at the smallest driving current and bubble formation at the sensing

electrodes. Under the circumstances, reliable read-outs could not be performed, although a comparison of the measured voltage before and after cell concentration revealed that a decrease in the range 35 to 50 mV, down from a typical maximum value of 2300 mV could be expected at high cell concentrations.

4.3.2 Sensing by Driving Current

Without sensing electrodes, the remaining option was using the integrated logging function of the power supply to record changes in voltage at a set driving current resulting from cell accumulation. Compilation according to Section 3.6.2.1 of the *S. cervisiae* and *E. coli* test series allowed graphing, as seen in Fig. 4.4, Fig. 4.5 and Fig. 4.6.

4.3.2.1 Concentration of *S. cervisiae*

S. cervisiae series 1 plotting results span a range from the lowest concentration known to produce an output signal ($2 \cdot 10^3$/ml) up to the highest multiple of 10 ($2 \cdot 10^6$/ml) obtainable by repeated blending with buffer after cell counting in the *Neubauer Chamber* (Section 3.5).

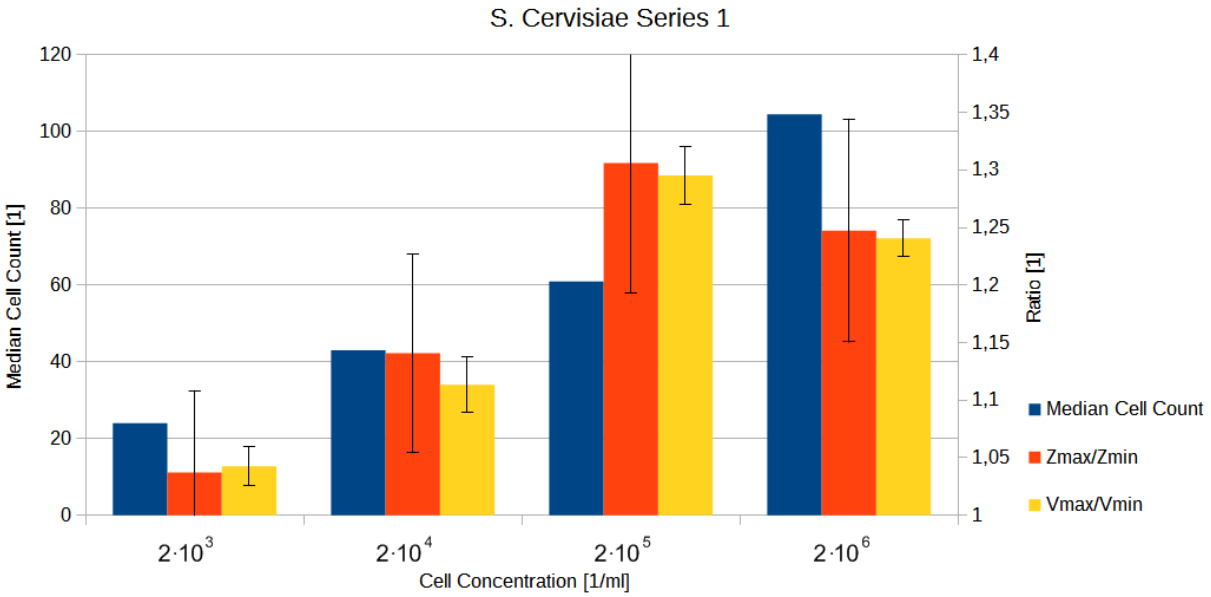

Figure 4.4: Comparing measured voltage, calculated impedance and optical cell count at varying cell concentration of *S. cervisiae*

Note that calculated impedance suffers from a crippling amount of deviation, while direct voltage measurements seem more reliable. A *Pearson* correlation coefficient (PCC) of 0.741

was observed in this data set comparing cell count and direct voltage measurement, with $p < 0.26$. Using calculated impedance the PCC is 0.730 and $p < 0.27$. Nevertheless, the impedance chart offers a simple means of control without requiring additional information, because a discrepancy to voltage measurement can point towards a compilation error.

S. cervisiae series 2 included larger reservoirs (with a diameter of 4 rather than 3 mm, nearly doubling the available sample volume), providing a larger amount of cells to work with at a given concentration as well as a high density test in the shape of undiluted sample, with $30 \cdot 10^6$ cells per ml. Reservoir size is primarily limited by the size of the PDMS pad surrounding the channel structure. Minimum concentration was halved to 10^6/ml from series 1, which barely registered in the output signal, despite the increase in available sample volume (Fig. 4.5).

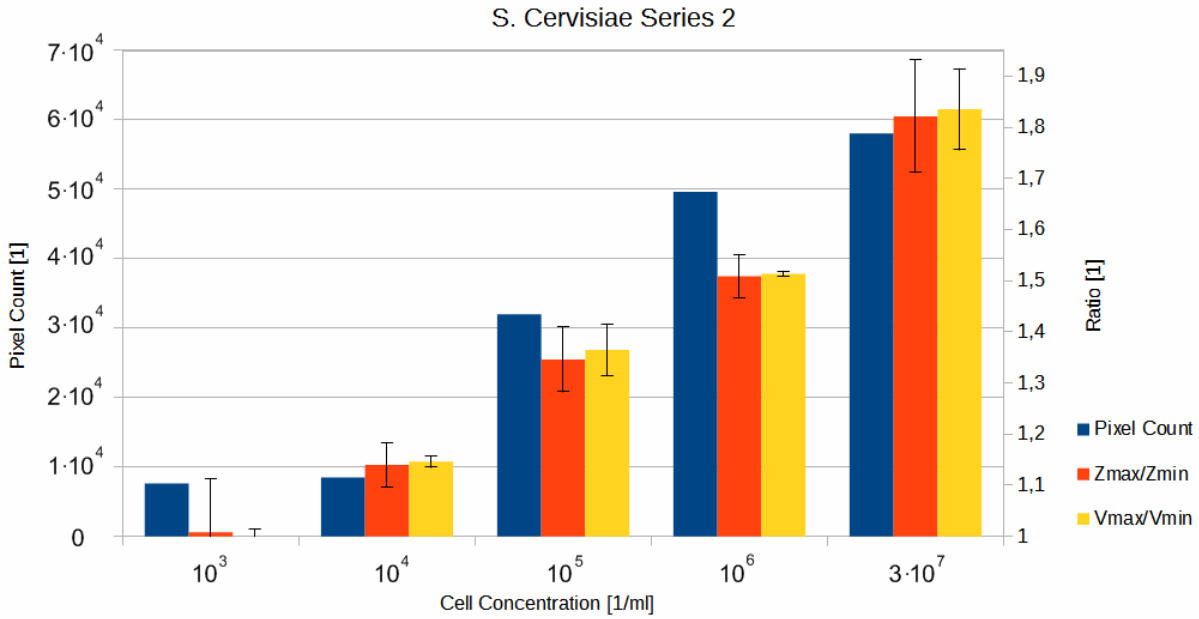

Figure 4.5: Comparing measured voltage, calculated impedance and the number of pixels occupied by cells of *S. cervisiae* in screen shots

Series two reference switched to pixel counting to take advantage of improved, which relies on marking cells with a unique color that is not at all present in the original image and using an image histogram. The observed PCC of measured voltage correlated with pixel count was 0.962 and $p < 8.8 \cdot 10^{-3}$, with calculated impedance the values were 0.964 and $p < 8.3 \cdot 10^{-3}$.

4.3.2.2 Concentration of *E. coli*

Tests with *E. coli* were performed with increased cell concentrations compared to those used for *S. cervisiae*, owing to their much smaller cell volume. To this end, the step size was increased to two orders of magnitude, spanning from 10^4/ml to 10^{10}/ml. This way, an output voltage range similar to the one observed in the *S. cervisiae* series was realized.

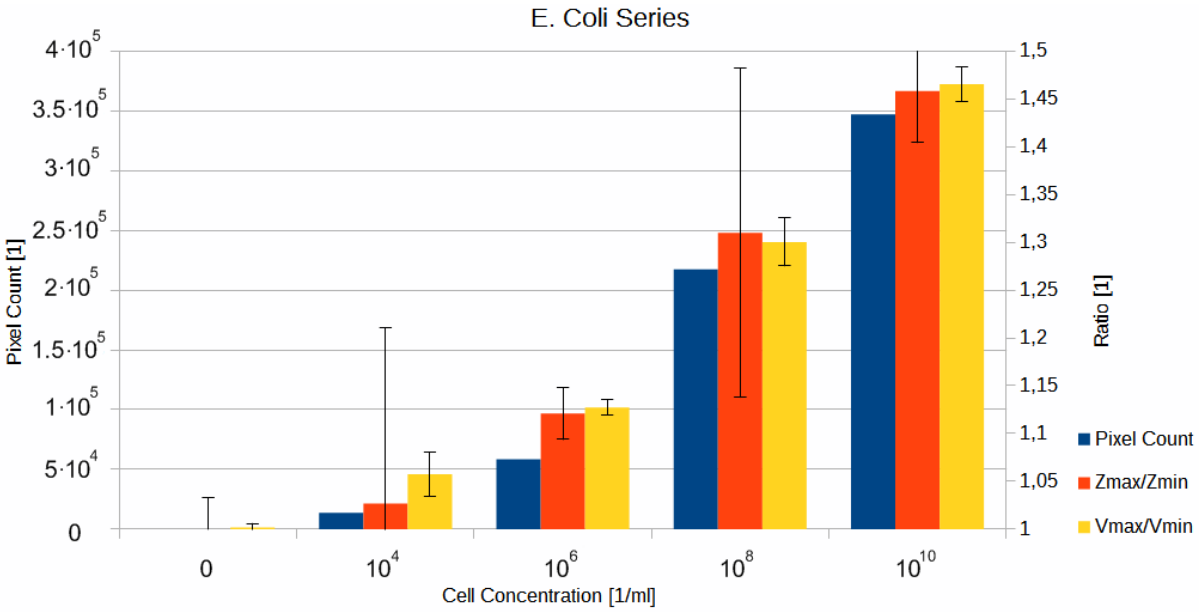

Figure 4.6: Comparing measured voltage, calculated impedance and the number of pixels occupied by cells of *E. coli*

The PCC from correlating pixel count and voltage in this case turned out to be 0.995 with $p < 0.44 \cdot 10^{-3}$, using impedance yields the same PCC but $p < 0.38 \cdot 10^{-3}$. One peculiarity of *E. coli* is that it forms sticky clusters (courtesy of their fimbriae [SCK01] [CBH+97]) at any concentration, which clog the nozzle and add a filtration effect. If accumulation is allowed to continue, the 'plug' thus created will keep growing from the base and start to extend beyond the nozzle (Fig. 4.2), until parts detach. Such behavior might prove advantageous for contact-less sensing in situ, but will impact any attempts at re-mobilization of the collected cell mass.

5 Conclusions

A type of microfluidic device for cell concentration and detection was created with an emphasis on the viability of target cells and preserving their mobility. The goal was achieved with cells exhibiting limited mutual adhesion (e.g. *S. cervisiae*), but less so in the case of cluster forming types (e.g. *E. coli*), whose aggregates tend to attach to channel walls and remain compounded even after detaching by inverted driving current. Whether this tendency will affect functionality depends on the type of the task at hand, a pure sensing application may even benefit from the increased density. All types of living cells used shared the same buffer electrolyte concentration (Section 4.2) for accumulation, while polysterene beads of sizes varying from 4 to 12 µm diameter needed minimal conductivity (sample emulsion diluted with de-ionized water by a factor of 1000). The device is very sensitive to changes in surface chemistry, including those caused by staining agents, whose residues have to be reduced as much as possible to preserve functionality.

Frequency based sensing via insulated surface deposited electrodes, as described in Section 3.4 and Section 4.3.1, would provide additional information compared to the simple longitudinal DC voltage measurement, but remained beyond the capabilities of insulating coating materials available for this work. Alternatively, there is a chance that a high frequency signal could be superimposed on the driving current to achieve a similar frequency selective capability without the use of additional electrodes. By comparison, limited testing with surface electrodes before breakdown occurred, showed that the signal maximum could be obtained at frequencies in the low MHz range (Section 4.3.1). This option would require a source capable of operating at similar frequencies, but at the same time provide the current and voltage levels needed to perform electrophoresis.

Using a regulated DC driving current, the detection method of choice proved to be longitudinal voltage measurement, which offered a better (smaller) average deviation than

calculated impedance, at least with the current source used in the course of this work (Section 3.6.1). The limit of detection and concentration required to generate an output signal of similar strength for *E. coli* was two and three orders of magnitude higher compared to that of *S. cervisiae*. Data shown here was derived with reservoirs holding between 12 and 20 µl, in which case 10^4 cells per ml for *S. cervisiae* and 10^6/ml for *E. coli* should be seen as the lower bound for detection (Section 4.3.2) when using the setup described here. An advantage of continuous operation is interruption-free processing of any amount of fluid with increasing runtime, which could help lower the threshold and increase the output signal strength, so long as the increased sample volume is available and can be stored within the module.

Concerning module production, the design proved well suited for PDMS, but the experience with dry film resist (DFR) components showed that large contact pads surrounding the channel structures are difficult to bond seamlessly and that *Ordyl SY330* is to coarse for the task. Additionally, since simpler versions provide the desired functionality, hydrogel barriers offer no advantage with this design and, by creating a parallel current path, also preclude the only type of electric measurement successfully employed so far, which is why this pathway should be avoided even if it became viable with improved DFR components or otherwise.

Insulating dedicated sensing electrodes against the voltages needed for electrophoresis turned out to be the most significant issue encountered during this work. Comparisons between liquid deposited polyimide coating with solid sheet (Section 4.3.1) indicated that mode of application rather than shortcomings of the material itself were responsible for the breakdowns. Addressing the susceptibility of even multi layered coatings to galvanic breakdown is apparently the key to employing impedimetric sensing via dedicated electrodes in such a setting. One way to avoid coatings altogether would be to laminate strips of thin sheet over sensing electrodes deposited on a glass slide, taking care to keep the contact pads exposed and accessible, if such a process can be developed.

Outlook

One key aspect, which needs to be explored, is the compatibility of the tested electrolyte concentration with various cell types. If, contrary to observations with the cell types tested here, strong variations in electrophoretic mobility exist, a controlled way of gradually increasing buffer concentrations could be devised, allowing to examine the more mobile ones first, which would then clear the constriction towards the anode once fluid conductivity

rises and EOF weakens, making way for less mobile specimen and such differences could be used to identify different target cells.

In its current state, the device only offers non-specific bulk detection of living cells and some form of electro-spectroscopic sensing remains highly desirable, but will require working electrode insulation or more capable hardware. Other methods, e.g. optical detection could be employed at the cost of increased complexity and only limited options, considering the known sensitivity of the device to staining dyes.

One aspect that might be of interest is the controlled extraction of already concentrated sample, which could be performed by tapping the cathode side channel and reversing driving current polarity while switching the anode to a third electrode located within the tap, once accumulation has taken place in normal operation. Such a setup would complicate priming immensely, however.

Appendix

A Datasheets

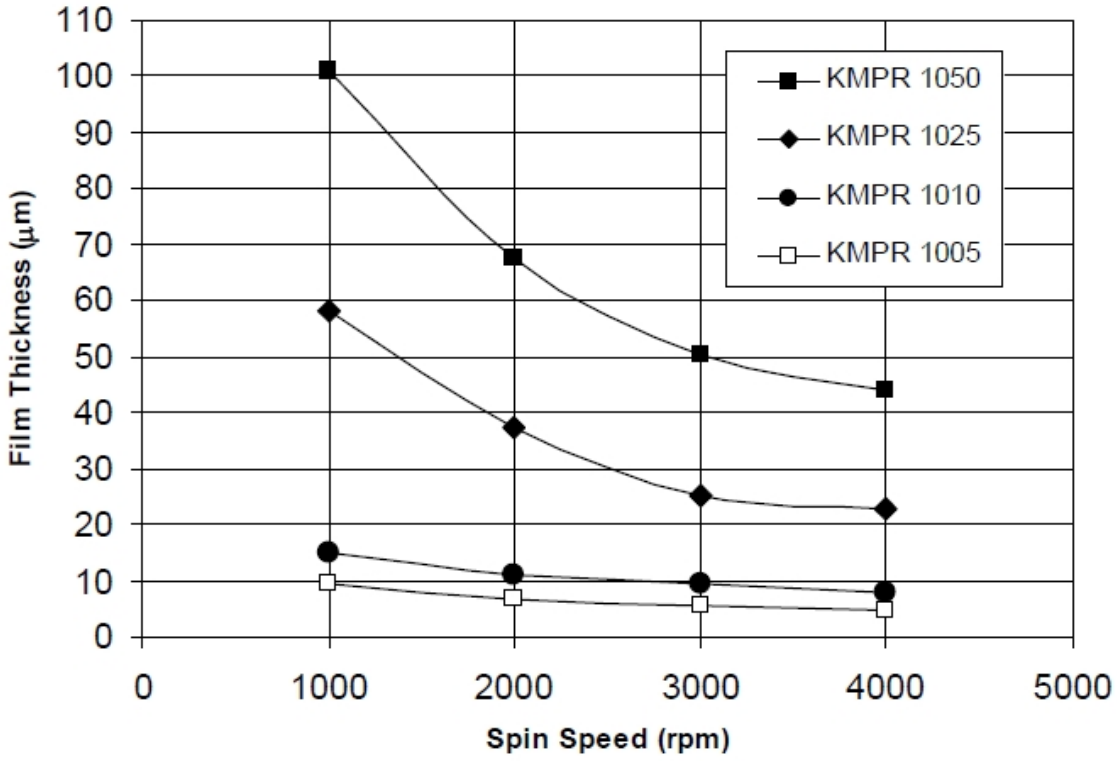

Figure 1. Spin speed vs. Thickness
for KMPR® 1000 resists (21°C US & EU)

Figure A1: Chart for determining *KMPR* spin resist thickness.

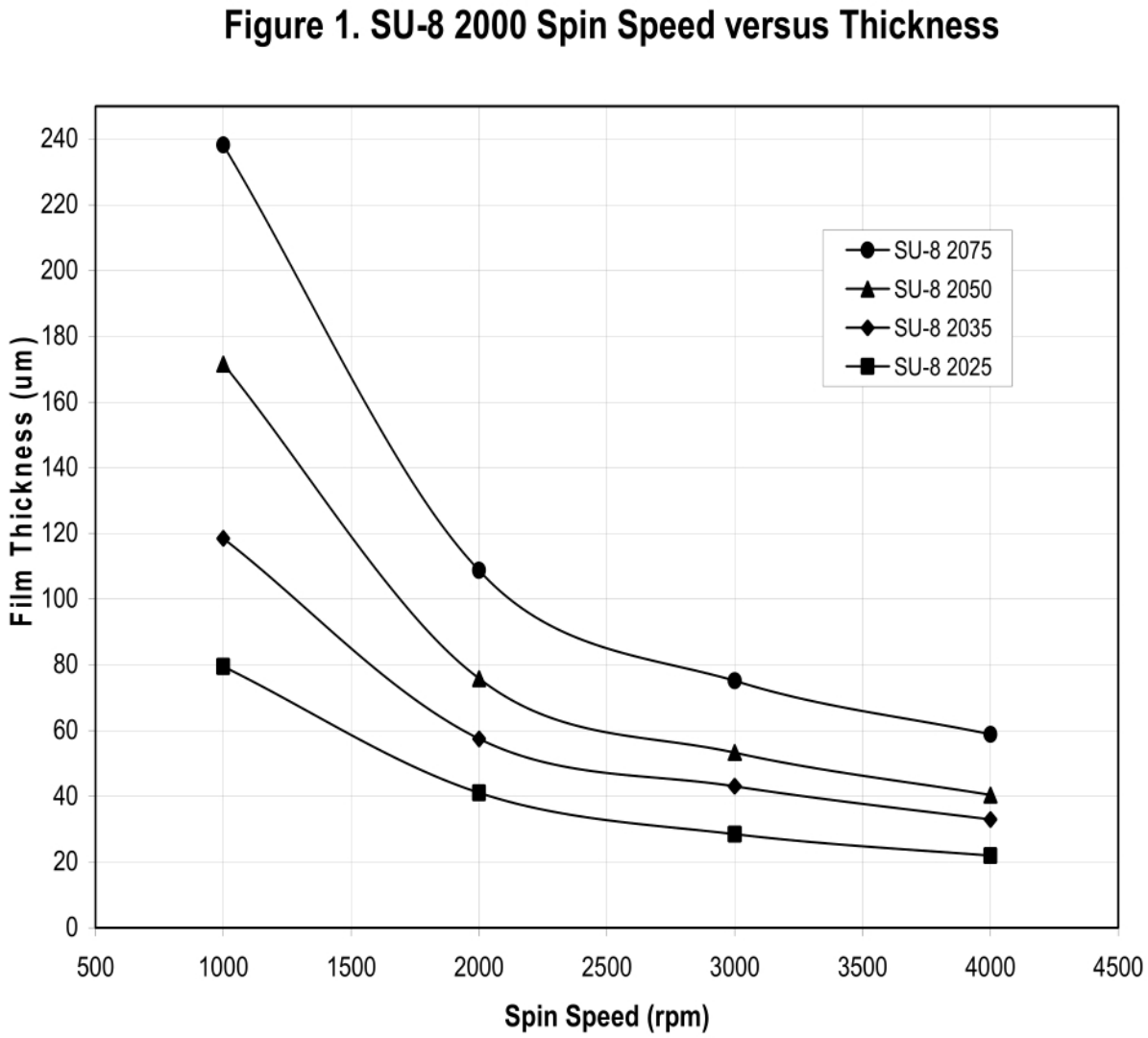

Figure A2: Chart for determining *SU-8* spin resist thickness.

B Amplifier Circuit Plan

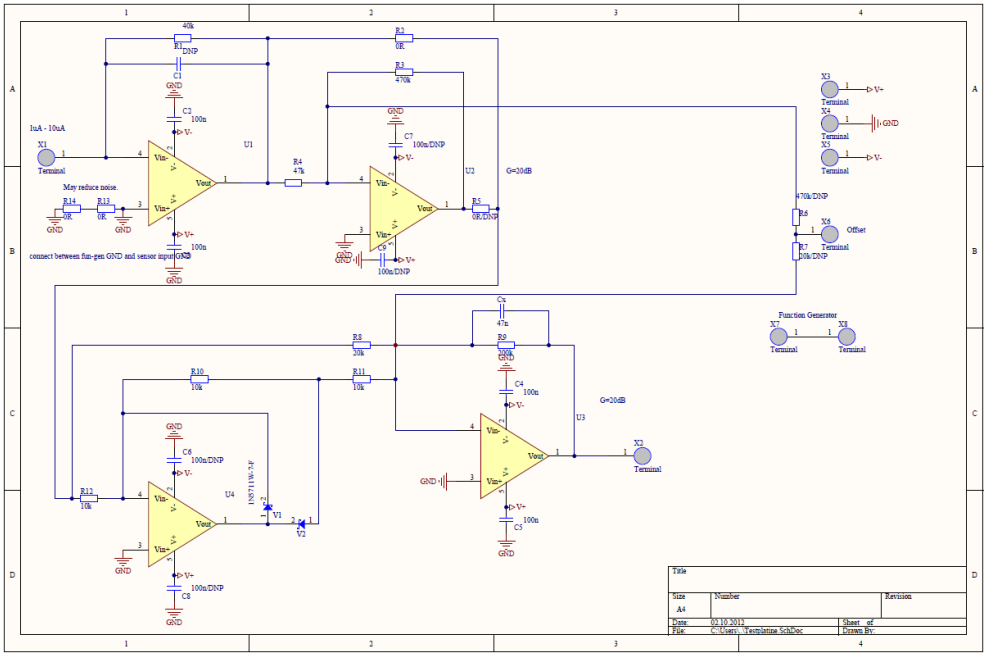

Figure B3: Sensing amplifier circuit plan.

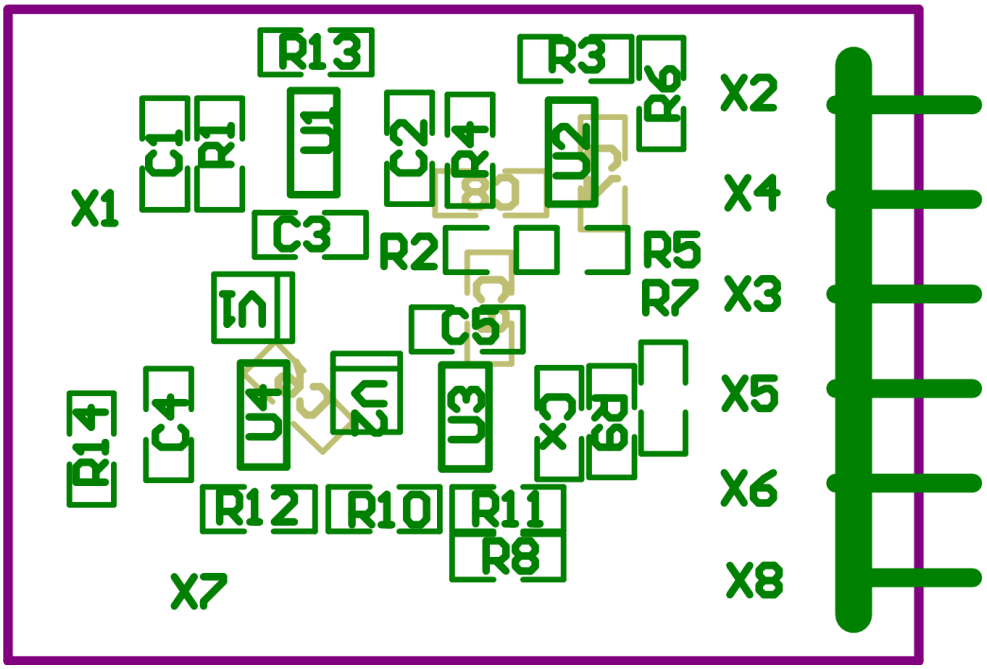

Figure B4: Sensing amplifier circuit board layout.

C Photo Masks

All masks except those used for top sandblasting come printed on a transparent A4 polymer sheet from the factory, with individual units the size of microscopic slides measuring 76 mm by 26 mm.

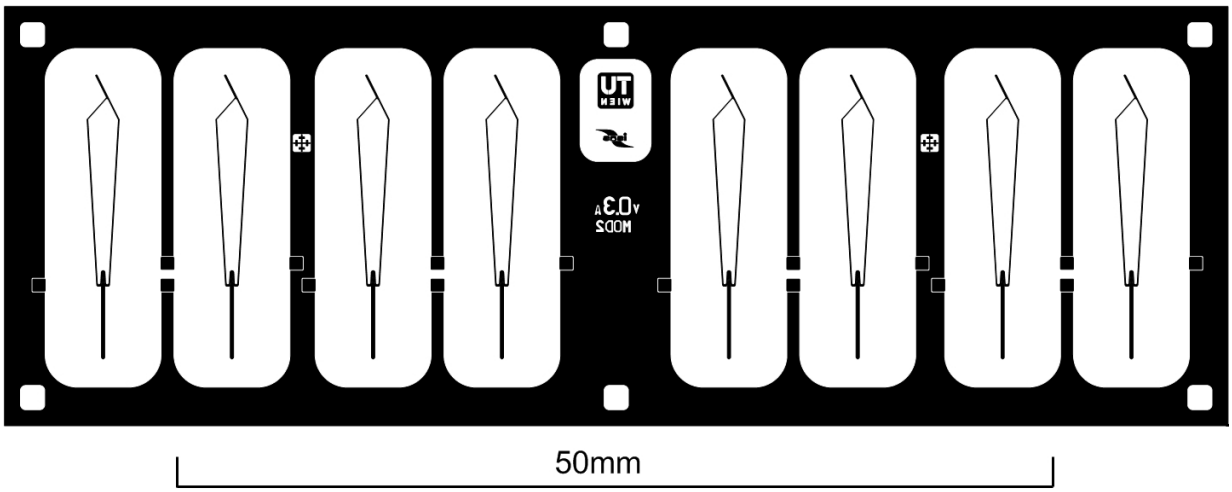

Figure C5: Dry film resist (DFR) photo mask for the bottom slide channel structures of the full length design. Note the horizontal inversion to bring the printed side in direct contact with the resist. Minimizing the distance between dyed layer and resist helps preserve resolution upon exposure. Rectangular pads around the periphery are for spacing, while the two smaller ones between modules contain alignment markers.

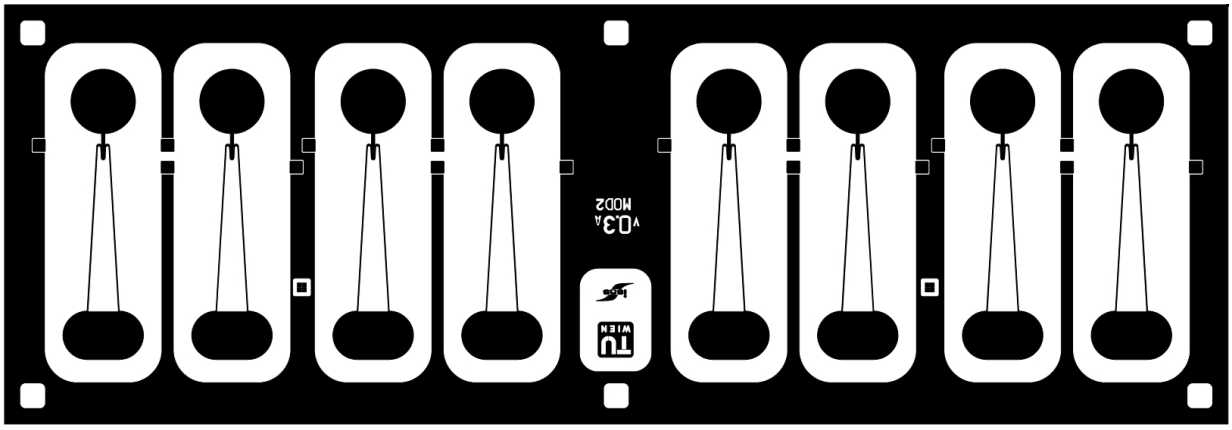

Figure C6: The full length top slide mask is also inverted vertically to allow alignment with the bottom half. Different reservoir shapes make identification of anode and cathode sides easier on the finished module.

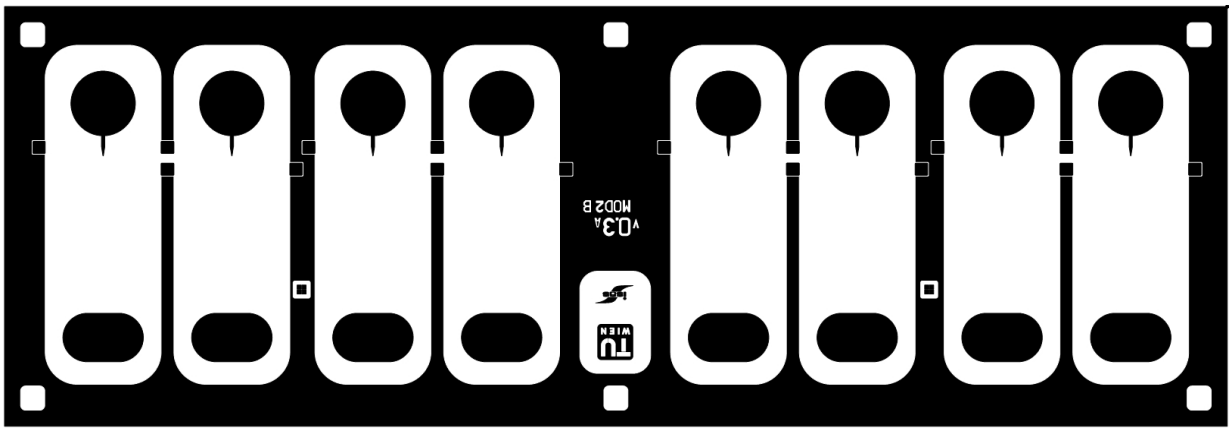

Figure C7: A modified top slide used for creating half-height feed channels, another variant can be made by using a blank top slide, for overall reduced channel depth.

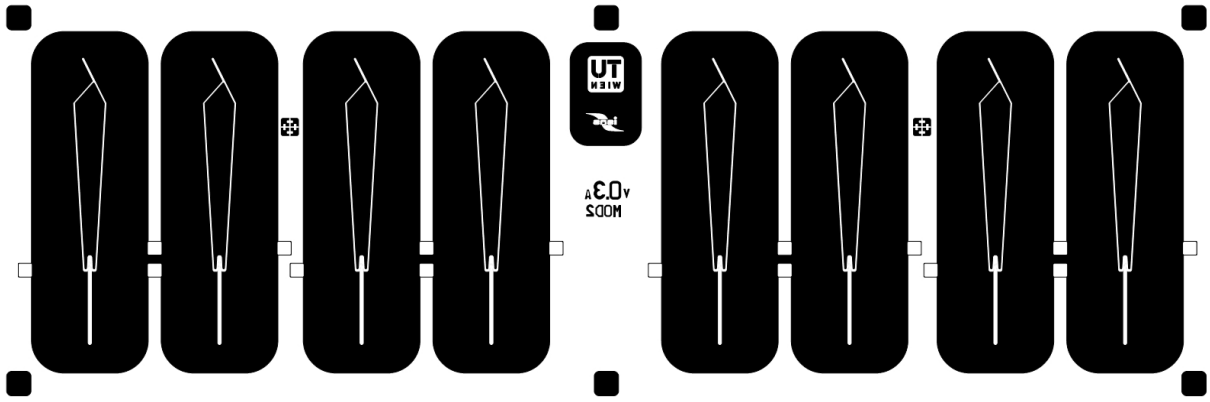

Figure C8: Inverted mask for creating PDMS molds of the long design from *Su-8* or *KMPR* spin resists. Unlike in sandwiched modules, only uniform channel height is available.

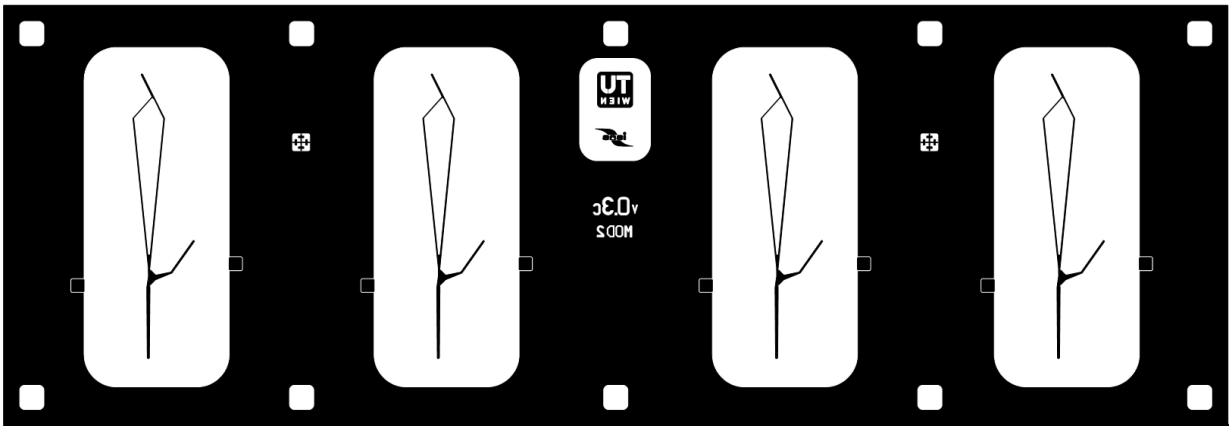

Figure C9: The bottom mask of the simpler hydrogel design needs a separate channel structure.

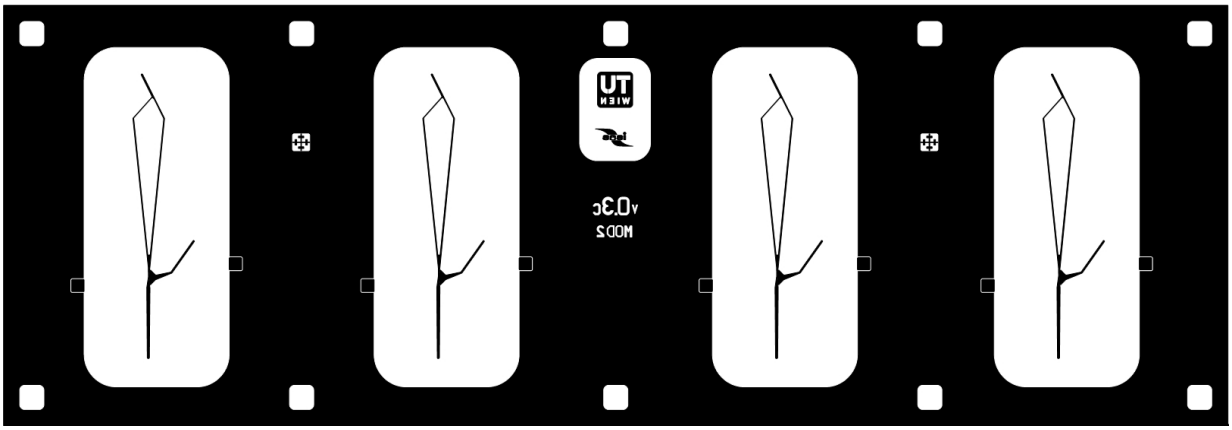

Figure C10: Unlike the dry designs, this one needs a top slide with structures to create a gap between phaseguide and opposing slide

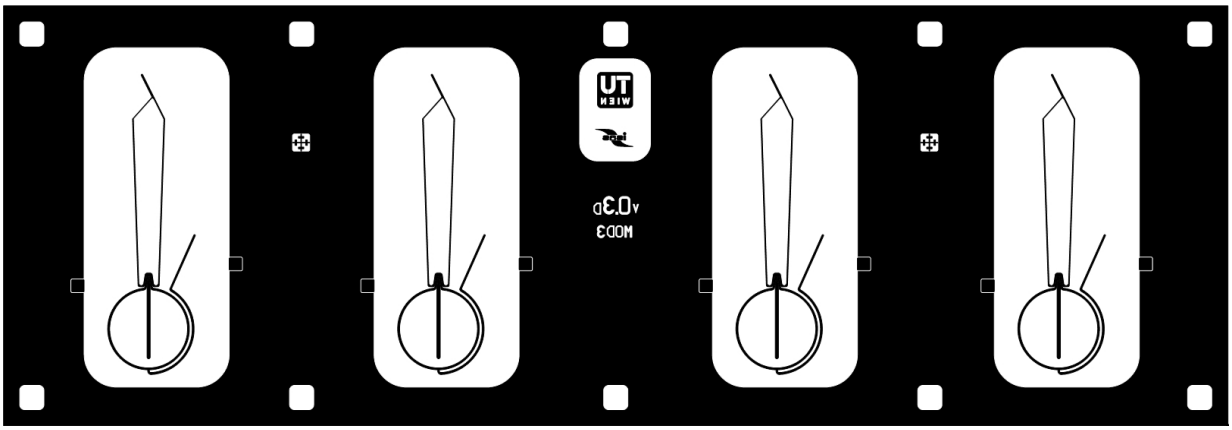

Figure C11: The 2nd hydrogel design is kept as closely as possible to the geometry of the dry designs. The bottom slide shown here mounts the phaseguides.

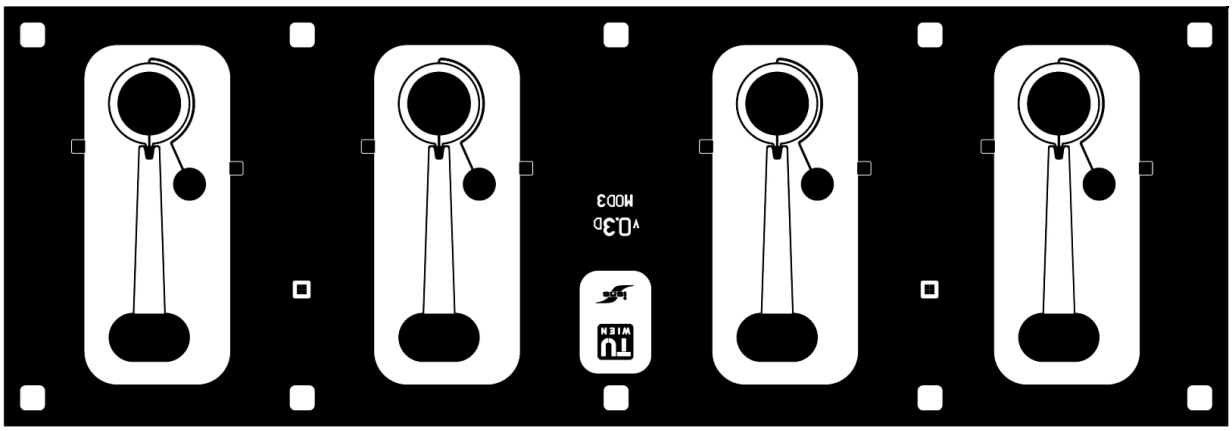

Figure C12: The top slide only contains a cavity covering the bottom structures from C11

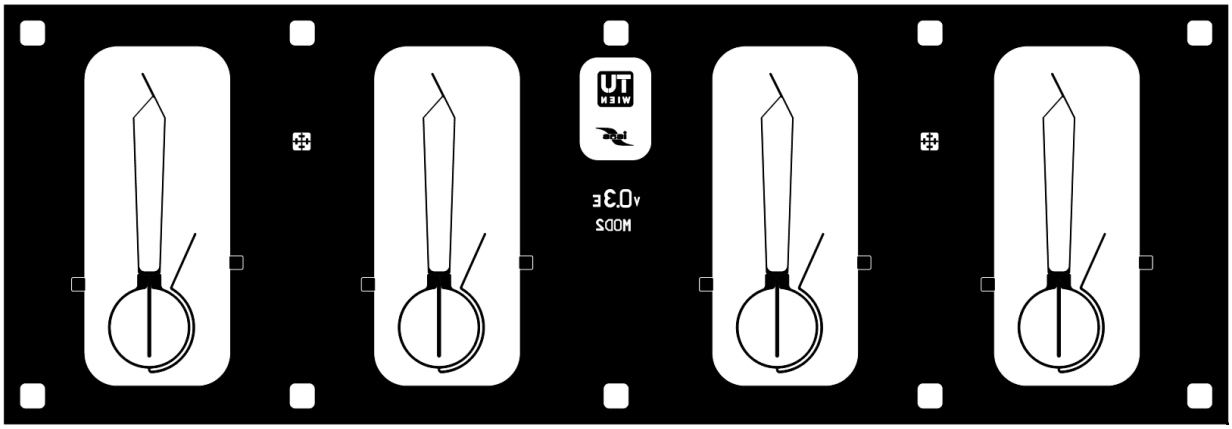

Figure C13: Bottom photo mask of a variation of the hydogel design from C11 with a larger gel part and greater differences to the dry designs. Straighter and shorter phaseguides are hoped to improve module reliability.

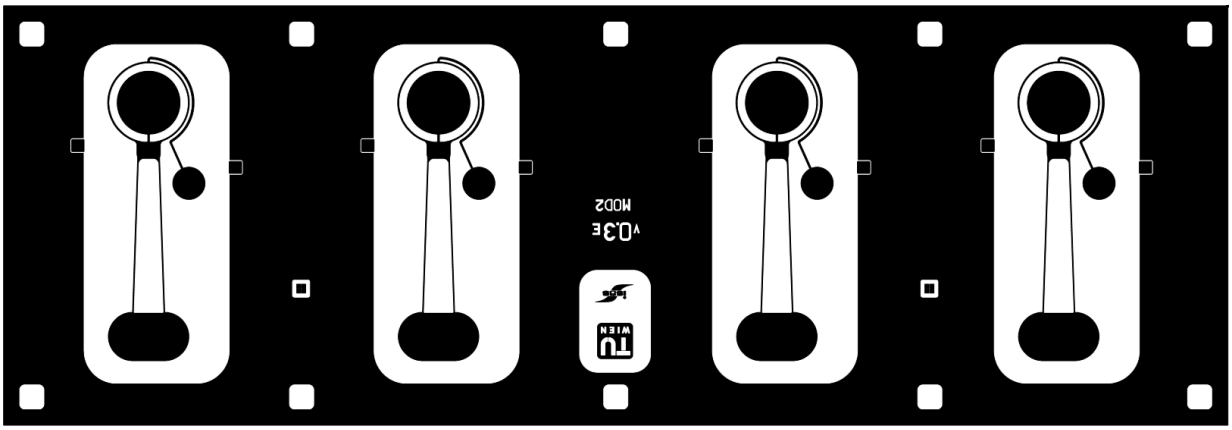

Figure C14: The top half is again only providing a cavity covering the bottom slide structures.

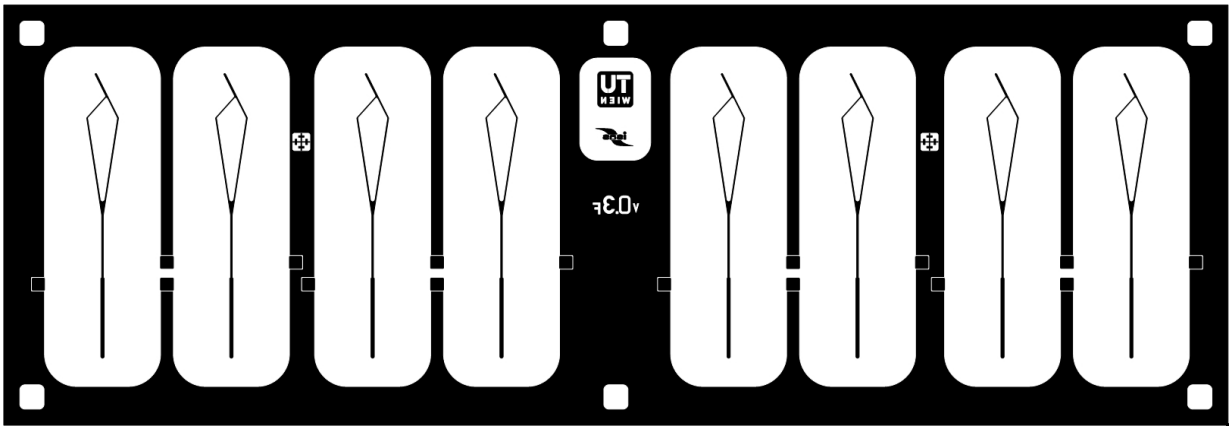

Figure C15: The vertical barrier design in dry film resist has a continuous but widening channel on the bottom slide.

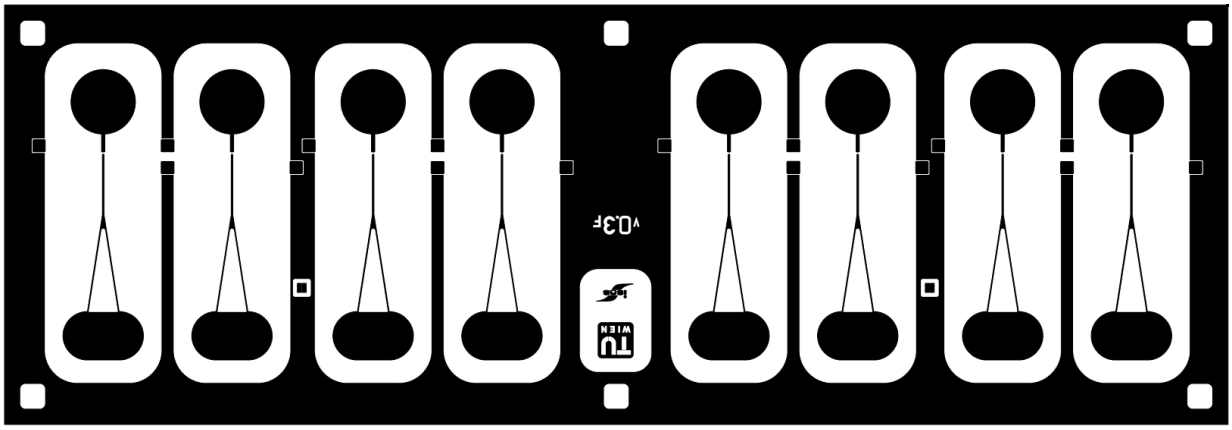

Figure C16: The top slide contains a barrier whose height can be changed by using a different gauge of DFR.

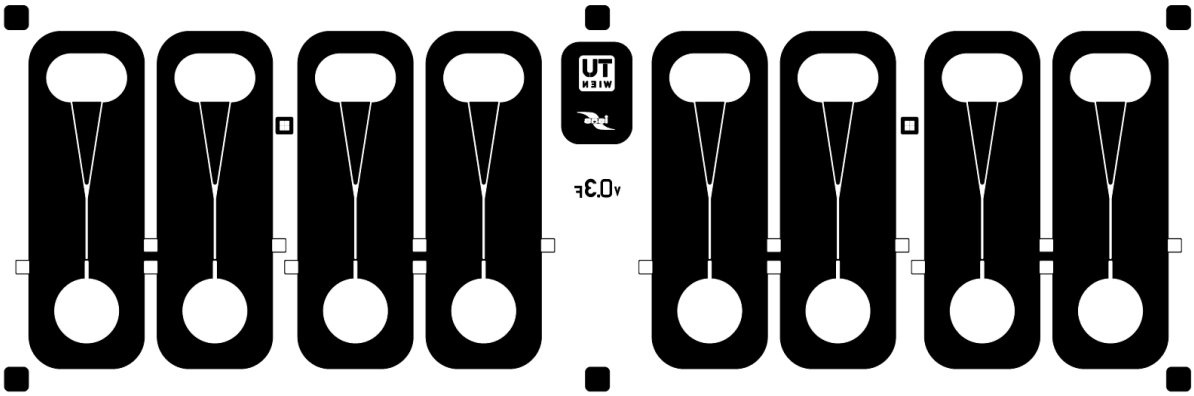

Figure C17: An inverted mask is again used for a PDMS mold of the vertical barrier design. A connecting channel has to be cut or machined into the substrate for the design to function.

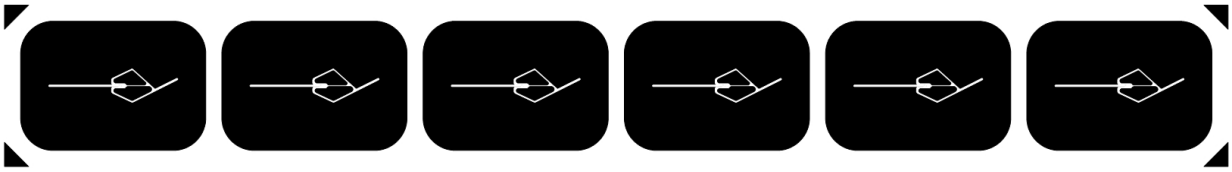

Figure C18: An inverted mask for a compact design made for PDMS only and originally intended for the bulk of pre-testing and calibration due to its smaller footprint. A full slide can be exposed at once by using two identical strips in parallel, a result of space constraints on the A4 sheet the masks were printed on. Note that punching the anode side reservoir into the tip of the cavity around the constriction in the long design from Fig. C8 can be used to create a functionally identical module.

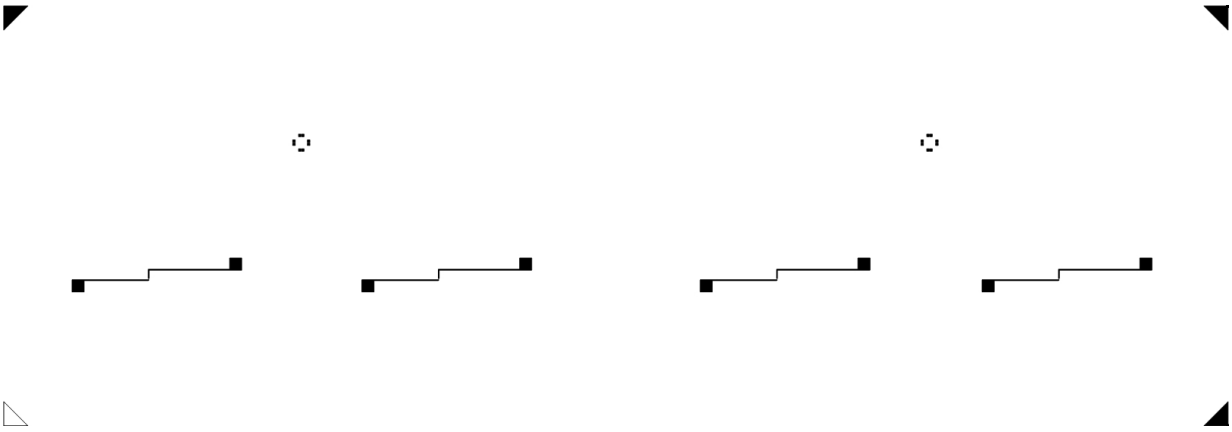

Figure C19: The photo mask used for creating widely spaced sensing electrodes is compatible with all hydrogel modules.

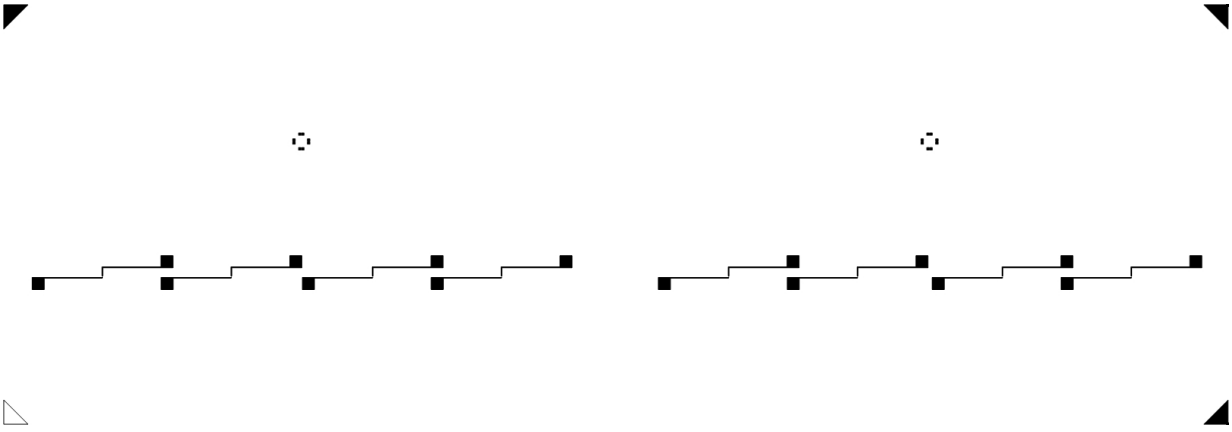

Figure C20: A narrow version of the sensing electrode mask for all non-hydrogel modules.

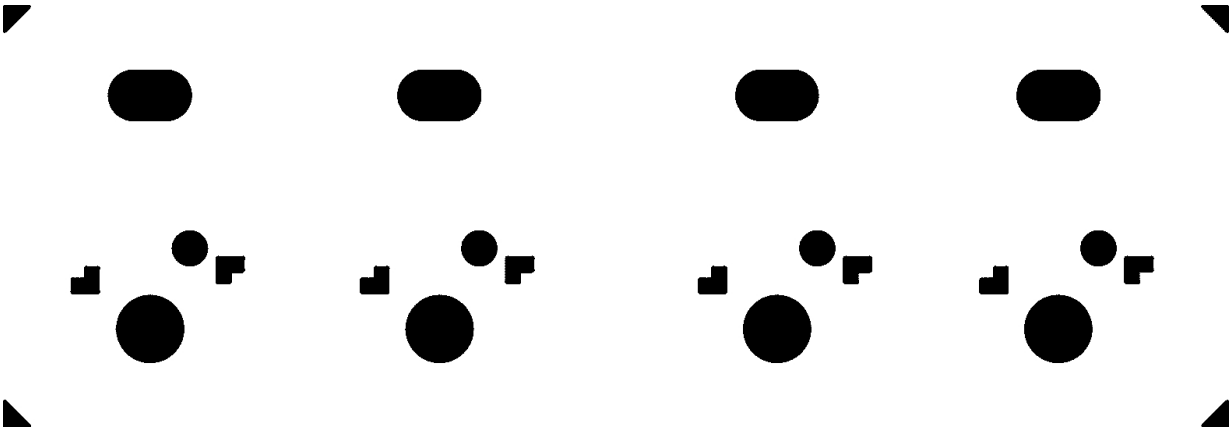

Figure C21: A perforation photo mask for top slides with wide spacing is compatible with all hydrogel based modules. This type of mask requires only limited resolution, so an ink-jet printer can be used. The small L-shaped openings provide access to contact pads beneath.

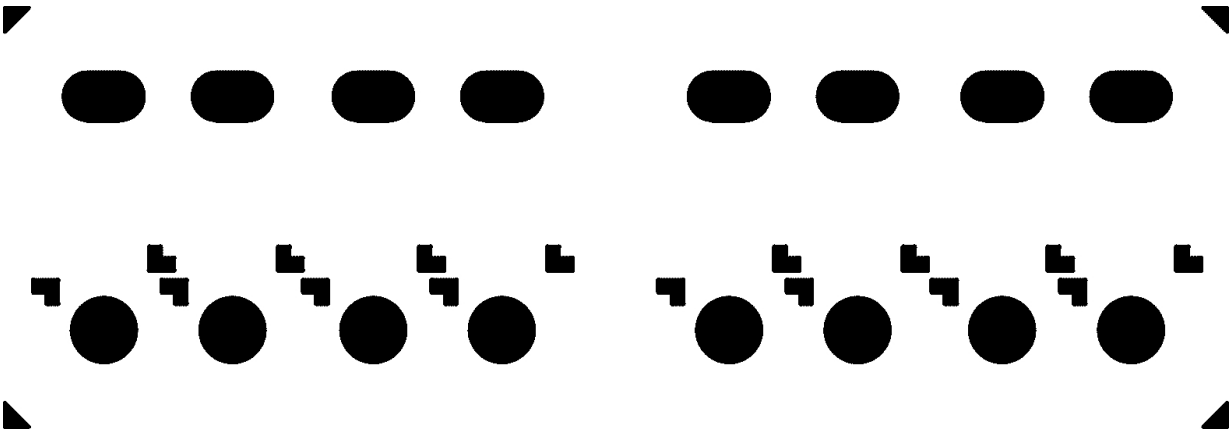

Figure C22: A perforation photo mask for top slides with narrow spacing, which is compatible with all dry film resist modules not employing hydrogel.

Literature

[AKS08] Adams, J. D. ; Kim, Unyoung ; Soh, H. T.: Multitarget Magnetic Activated Cell Sorter. In: *PNAS* 105 No.47 (2008), pp. 18165–18170

[Aut14] Autodesk Inc.: AutoDESK Design Suite website, visisted Sept. 27th. 2014. – http://www.autodesk.com/products

[BK04] Brody, Jonathan R. ; Kern, Scott E.: Sodium Boric Acid: a Tris-free, Cooler Conductive Medium for DNA Electrophoresis. In: *BioTechniques* 36 (2004), pp. 214–216

[Bri31] Bridgman, P.W.: *Dimensional Analysis*. New Haven, USA : Yale University Press, 1931

[Buc14] Buckingham, E.: On Physically Similar Systems, Illustration of the Use of Dimensional Equations. In: *Phys. Rev.* 4 (1914), pp. 345–376

[CBH+97] Czeczulin, John R. ; Balepur, Shyam ; Hicks, Susan ; Phillips, Alan ; Hall, Robert ; Kothary, Mahendra H. ; Navarro-Garcia, Fernando ; Nataro, James P.: Aggregative Adherence Fimbria II, a Second Fimbrial Antigen Mediating Aggregative Adherence in Enteroaggregative Escherichia coli. In: *Infection and Immunity* 65 (1997), pp. 4135–4145

[CCST10] Chang, Feng-Ming ; Chang, Yi-Wen ; Sheng, Yu-Jane ; Tsao, Heng-Kwong: Size-Dependent Electro-Osmosis in a Microchannel with Low-Permittivity, Salt-Free Media. In: *Applied Physics Letters* 97 (2010), pp. 164101

[Cel14] Celeromics S.A.: Online Neubauer Chamber Manual, visisted Oct

6th. 2014. – http://celeromics.com/en/resources/docs/Articles/Cell-counting-Neubauer-chamber.pdf

[Cha05] Chakrabarty, Krishnendu: Design, Testing, and Applications of Digital Microfluidics-Based Biochips. In: *Proceedings of the 18th International Conference on VLSI Design*, 2005

[Cla14] Clariant Corp.: Online AZ 5214 E datasheet, visisted Oct. 15th. 2014. – http://www.microchemicals.com/micro/az_5214e.pdf

[CLC+11] Chin, C.D. ; Laksanasopin, T. ; Cheung, Y.K. ; Steinmiller, D. ; Linder, V. ; Parsa, H. ; Wang, J. ; Moore, H. ; Rouse, R. ; Umviligihozo, G. ; Karita, E. ; Mwambarangwe, L. ; Braunstein, S.L. ; Wijgert, J. van d. ; Sahabo, R. ; Justman, J.E. ; El-Sadr, W. ; Sia, S.K.: Microfluidics-Based Diagnostics of Infectious Diseases in the Developing World. In: *Nature Medicine* 17 (2011), pp. 1015

[COM14] COMSOL Inc.: COMSOL Multiphysics website, visisted Sept. 19th. 2014. – http://www.comsol.com/products

[CP07] Choi, Sungyoung ; Park, Je-Kyun: Continuous Hydrophoretic Separation and Sizing of Microparticles Using Slanted Obstacles in a Microchannel. In: *Lab on a Chip* 7 (2007), pp. 890–897

[CZH+10] Church, Christopher ; Zhu, Junjie ; Huang, Guohui ; Tzeng, Tzuen-Rong ; Xuan, Xiangchun: Integrated Electrical Concentration and Lysis of Cells in a Microfluidic Chip. In: *Biomicrofluidics* 4 (2010), pp. 0441011–10

[Dow14] Dow Corning Corp.: Online Sylgard 184 Datasheet, visisted Sept 29th. 2014. – http://www.dowcorning.com/applications/search/products/details.aspx?prod=01064291&type=PROD

[GJZ+12] Gu, Congying ; Jia, Zhijian ; Zhu, Zaifang ; He, Chiyang ; Wang, Wei ; Morgan, Aaron ; Lu, Joann J. ; Liu, Shaorong: Miniaturized Electroosmotic Pump Capable of Generating Pressures of More than 1200 Bar. In: *Analytical Chemistry* 84 (2012), pp. 9609–9614

[HAR15] HARKE Services GmbH: Harke I-XE Datasheet, visited Jul. 24th. 2015. – http://www.harke.com/fileadmin/images/imaging/PDF-2012/UserGuide_APM_I-XE.pdf

[HEB+06] Heng, X. ; Erickson, D. ; Baugh, L.R. ; Yaqoob, Z. ; Sternberg, P.W. ; Psaltis, D. ; Yang, C.H.: Optofluidic Microscopy - a Method for Implementing a High Resolution Optical Microscope on a Chip. In: *Lab on a Chip* 6 (2006), pp. 1274–1276

[HF05] Han, Ki-Ho ; Frazier, A. B.: Diamagnetic Capture Mode Magnetophoretic Microseparator for Blood Cells. In: *Journal of Microelectromechanical Systems* 14 (2005), pp. 1421–1431

[Jon95] Jones, T.B.: *Electromechanics of Particles*. Cambridge, MA, USA : Cambridge University Press, 1995

[Ker07] Kerkhoff, H.G.: Testing Microelectronic Biofluidic Systems. In: *Design and Test of Computers, IEEE* 24 No. 1 (2007), pp. 72–82

[Lab14] LabSmith Inc: Lab Smith website, visisted Oct 14th. 2014. – http://labsmith.com/products/LabSmith_HVS448_brochure_2011_2012.pdf

[LAF+14] Li, Yongxin ; Afrasiabi, Rouzbeh ; Fathi, Farkhondeh ; Wang, Nan ; Xiang, Cuili ; Lov, Ryan ; She, Zhe ; Kraatz, Heinz-Bernhard: Impedance Based Detection of Pathogenic E. coli O157:H7 Using a Ferrocene-Antimicrobial Peptide Modified Biosensor. In: *Biosensors and Bioelectronics* 58 (2014), pp. 193–199

[LQO+09] Liu, C. ; Qiu, X. ; Ongagna, S. ; Chen, D. ; Chen, Z. ; Abrams, W.R. ; Malamud, D. ; Corstjens, P.L.A.M. ; Bau, H.H.: A Timer-Actuated Immunoassay Cassette for Detecting Molecular Markers in Oral Fluids. In: *Lab on a Chip* 9 (2009), pp. 768

[LT99] Lee, Sang-Wook ; Tai, Yu-Chong: A Micro Cell Lysis Device. In: *Sensors and Actuators* 73 (1999), pp. 74–79

[Mic14a] Microchem Corp.: Online SU-8 2000 Datasheet, visisted May 14th. 2014. – http://www.microchem.com/pdf/SU-82000DataSheet2025thru2075Ver4.pdf

[Mic14b] Microchem Corp.: Online KMPR Datasheet, visisted Oct. 14th. 2014. – http://microchem.com/pdf/KMPRDataSheetver4_2a.pdf

[MMP97] Madigan, M.T. ; Martinko, J.M. ; Parker, J.: *Brock Biology of Microor-*

ganisms. Hertfordshire, UK : Prentice Hall International, 1997

[NMF+09] Neirinck, Bram ; Mellaert, Lieve V. ; Fransaer, Jan ; der Biest, Omer V. ; Anne, Jozef ; Vleugels, Jef: Electrophoretic Deposition of Bacterial Cells. In: *Electrochemistry Communications* 11 (2009), pp. 1842–1845

[PEPH+11] Puchberger-Enengl, Dietmar ; Podszun, Susann ; Heinz, Helene ; Hermann, Carsten ; Vulto, Paul ; Urban, G. A.: Microfluidic Concentration of Bacteria by On-Chip Electrophoresis. In: *Biomicrofluidics* 5 (2011), pp. 0441111–10

[Pet10] Pethig, Ronald: Dielectrophoresis: Status of the Theory, Technology and Application. In: *Biomicrofluidics* 4 (2010), pp. 022811

[Pic14] Pico Techology Inc: Pico Log Website, visisted Oct 14th. 2014. – http://www.picotech.com/document/brochures.html?id=44

[Poh51] Pohl, H. A.: The Motion and Precipitation of Suspensoids in Divergent Electric Fields. In: *Journal Of Applied Physics* 22 (1951), pp. 869

[PS13] Pethig, Ronald ; Smith, Steward: *Introductory Bioelectronics: For Engineers and Physical Scientists*. Hertfordshire, UK : John Wiley and Sons, Ltd, 2013

[PVH+12] Podszun, S. ; Vulto, P. ; Heinz, H. ; Hakenberg, S. ; Hermann, C ; Hankemeier, T ; Urbana, G.A.: Enrichment of Viable Bacteria in a Micro-Volume by Free-Flow Electrophoresis. In: *Lab on a Chip* 12 (2012), pp. 451–457

[PW97] Pfetsch, A. ; Welsch, T.: Determination of the Electrophoretic Mobility of Bacteria and their Separation by Capillary Zone Electrophoresis. In: *Analytical and Bioanalytical Chemistry* 359 (1997), pp. 198–201

[QN08] Qian, X.-M. ; Nie, S. M.: Single-Molecule and Single-Nanoparticle SERS: from Fundamental Mechanisms to Biomedical Applications. In: *Chem. Soc. Rev.* 37 (2008), pp. 912–920

[RA05] Radke, Stephen M. ; Alocilja, Evangelyn C.: A Microfabricated Biosensor for Detecting Foodborne Bioterrorism Agents. In: *IEEE Sensors Journal* 5

No. 4 (2005), pp. 744–750

[RLH+11] Rivet, Catherine ; Lee, Hyewon ; Hirsch, Alison ; Hamilton, Sharon ; Lu, Hang: Microfluidics for Medical Diagnostics and Biosensors. In: *Chemical Engineering Science* 66 (2011), pp. 1490–1507

[RMW95] Raymond, D. E. ; Manz, Andreas ; Widmer, H. M.: Continuous Sample Preparation Using Free-Flow Electrophoresis on a Silicon Microstructure. In: *Transducers '95 - Eurosensors IX*, 1995

[RRDB12] Roy, Pranab ; Rahaman, Hafizur ; Dasgupta, Parthasarthi ; Bhattacharya, Bhargab B. B.: A New Look Ahead Technique for Customized Testing in Digital Microfluidic Biochips. In: *2012 IEEE 21st Asian Test Symposium*, 2012

[RZA12] Rios, Angel ; Zougagh, Mohammed ; Avila, Monica: Review: Miniaturization Through Lab-on-a-Chip: Utopia or Reality for Routine Laboratories? In: *Analytica Chimica Acta* 740 (2012), pp. 1–11

[SAHZ13] Shukla, Vineeta ; Ali, Noohul Basheer Z. ; Hussin, Fawnizu A. ; Zwolinski, Mark: On Testing of MEDA Based Digital Microfluidics Biochips. In: *5th Asia Symposium on Quality Electronic Design*, 2013

[SCK01] Schembri, Mark A. ; Christiansen, Gunna ; Klemm, Per: FimH-mediated Autoaggregation of Escherichia Coli. In: *Molecular Microbiology* 41 (2001), pp. 1419–1430

[SERL03] Sze, Alice ; Erickson, David ; Ren, Liqing ; Li, Dongqing: Zeta-Potential Measurement Using the Smoluchowski Equation and the Slope of the Current-Time Relationship in Electroosmotic Flow. In: *Journal of Colloid and Interface Science* 261 (2003), pp. 402–410

[Sig14] Sigma-Aldrich Corp.: Mowiol 4-88 Datasheet, visisted Nov. 27th. 2014. – http://www.sigmaaldrich.com

[SL05] Su, Xiao-Li ; Li, Yanbin: A QCM Immunosensor for Salmonella Detection with Simultaneous Measurements of Resonant Frequency and Motional Resistance. In: *Biosensors and Bioelectronics* 21 (2005), pp. 840–848

[SLR72] Sherbet, G. V. ; Lakshmi, M. S. ; Rao, K. V.: Characterisation of Ionogenic

Groups and Estimation of the Net Negative Electric Charge on the Surface of Cells Using Natural pH Gradients. In: *Experimental Cell Research* 70 (1972), pp. 113–123

[SM10] Sun, T. ; Morgan, H.: Single-Cell Microfluidic Impedance Cytometry: a Review. In: *Microfluidics and Nanofluidics* 8 (2010), pp. 423–443

[SNO+12] Schumacher, Soeren ; Nestler, Joerg ; Otto, Thomas ; Wegener, Michael ; Ehrentreich-Foerster, Eva ; Michel, Dirk ; Wunderlich, Kai ; Palzer, Silke ; Sohn, Kai ; Weber, Achim ; Burgard, Matthias ; Grzesiak, Andrzej ; Teichert, Andreas ; Brandenburg, Albrecht ; Koger, Birgit ; Albers, Joerg ; Nebling, Eric ; Bier, Frank F.: Highly-Integrated Lab-on-Chip System for Point-of-Care Multiparameter Analysis. In: *Lab on a Chip* 12 (2012), pp. 464–473

[Son01] Sonin, A.A.: *The Physical Basis of Dimensional Analysis*. Cambridge, MA, USA : MIT, 2001

[Spu92] Spurk, Joseph H.: *Dimensionsanalyse in der Stroemungslehre*. Berlin, FRG : Springer, 1992

[VGA+05] Vulto, P. ; Glade, N. ; Altomare, L. ; Bablet, J. ; Tin, L. D. ; Medoro, G. ; Chartier, I. ; Manaresi, N. ; Tartagnia, M. ; Guerrieri, R.: Microfluidic Channel Fabrication in Dry Film Resist for Production and Prototyping of Hybrid Chips. In: *Lab on a Chip* 5 (2005), pp. 158–162

[VK08] Vig, Asger L. ; Kristensen, Anders: Separation Enhancement in Pinched Flow Fractionation. In: *Applied Physics Letters* 93 (2008), pp. 203507

[VL09] Varshney, Madhukar ; Li, Yanbin: Interdigitated Array Microelectrodes Based Impedance Biosensors for Detection of Bacterial Cells. In: *Biosensors and Bioelectronics* 24 (2009), pp. 2951–2960

[VXL06] Venditti, Roberto ; Xuan, Xiangchun ; Li, Dongqing: Experimental Characterization of the Temperature Dependence of Zeta Potential and its Effect on Electroosmotic Flow Velocity in Microchannels. In: *Microfluid. Nanofluid.* 2 (2006), pp. 493–499

[WCW07] Wang, Xianming ; Chien, Bo ; Wu, Jiankang: A Semianalytical Solution of Periodical Electro-Osmosis in a Rectangular Microchannel. In: *Physics of*

Fluids 19 (2007), pp. 127101

[YIB06] Yoshina-Ishii, Chiaki ; Boxer, Steven G.: Controlling Two-Dimensional Tethered Vesicle Motion Using an Electric Field: Interplay of Electrophoresis and Electro-Osmosis. In: *Langmuir* 22 (2006), pp. 2384–2391

[Zit14] Zitzmann GmBH: Zitzmann GmBH. website, visisted Oct 9th. 2014. – http://www.zitzmann-gmbh.de/index.php?id=121

[ZT06] Zheng, Siyang ; Tai, Yu-Chong: Design and Fabrication of a Micro Coulter Counter with Thin Film Electrodes. In: *Proceedings of 2006 lnternational Conference on Microtechnologies in Medicine and Biology, Okinawa*, 2006